

Impact of distributed meteorological forcing on ^{AUT:}simulated snow cover and ^{AUT:}simulated hydrological fluxes over a mid-elevation alpine micro-scale catchment

Aniket Gupta¹, Alix Reverdy¹, Jean-Martial Cohard¹, Basile Hector¹, Marc Descloitres¹, Jean-Pierre Vandervaere¹, Catherine Coulaud¹, Romain Biron¹, Lucie Liger², Reed Maxwell³, Jean-Gabriel Valay², and Didier Voisin¹

¹Univ. Grenoble Alpes, CNRS, IRD, Institut des Géosciences de l'Environnement (IGE), UMR 5001, Grenoble, France

²Université Grenoble Alpes, CNRS, Lautaret, F-38000, Grenoble, France

³Department of Civil and Environmental Engineering, Princeton University, Princeton, NJ, USA

Correspondence: Aniket Gupta (aniket.gupta@univ-grenoble-alpes.fr)

Abstract. From the micro to mesoscale, water and energy budgets of mountainous catchments are largely driven by topographic features such as terrain orientation, slope, steepness, and elevation together with associated meteorological forcings such as precipitation, solar radiation, and wind speed. ^{AUT:}~~This impacts~~It governs the snow deposition, melting, and transport, which further impact the overall water cycle. However, this microscale variability is not well represented in Earth System Models due to coarse resolutions. ^{AUT:}~~Moreover, the impact of resolution on the simulated water and energy balance lacks quantification.~~ This study explores the impact of precipitation, shortwave radiation and wind speed on the water budgets ^{AUT:}distribution over a 15.28 ha small mid-elevation (2000-2200 m) alpine catchment at Col du Lautaret (France). The grass dominated catchment remains covered with snow for 5 to 6 months per year. The surface-subsurface coupled ^{AUT:}~~hyper-resolution (10 m)~~ distributed hydrological model ParFlow-CLM is used ^{AUT:}at very high resolution (10m) to simulate the impacts ^{AUT:}on the water cycle of meteorological variability at ^{AUT:}~~spatio-temporal micro-scale~~very small spatial and temporal scale^{AUT:}on the water cycle. These include 3D simulations of hydrological fluxes with spatially distributed forcing of precipitation, shortwave radiation, and wind speed compared to 3D simulations of hydrological fluxes with non-distributed forcing. Our precipitation distribution method encapsulates spatial snow distribution along with snow transport. The model simulates the dynamics and spatial variability of snow cover using the ^{AUT:}~~CLM~~Common Land Model (CLM) energy balance module and under different combinations of distributed forcing. The resulting subsurface and surface water transfers are ^{AUT:}~~solved~~computed by the ParFlow module. Distributed forcing leads to spatially heterogeneous snow cover simulation, which becomes patchy at the end of the melt season and shows a good agreement with the remote sensing images (^{AUT:}~~MBE~~Mean Bias Error (MBE) = 0.22). This asynchronous melting results in a longer melting period compared to the non-distributed forcing, which does not generate any patchiness^{AUT:}~~(MBE = 0.6, -0.4)~~. Among the distributed meteorological forcings tested, precipitation distribution, including snow transport, has the greatest impact on spatial snow cover (MBE = 0.06) and runoff. Shortwave radiation distribution has an important impact on reducing evapotranspiration as a function of the slope orientation (decrease in ^{AUT:}~~regression slopes~~slope between observed and simulated evapotranspiration from 1.55 to 1.18). For the primarily east-facing ^{AUT:}~~watershed~~catchment ^{AUT:}~~studies~~studied here, ^{AUT:}~~the distribution of shortwave radiation adds a small differential snowmelt with~~distributing shortwave radiations helps generating realistic timing and spatial heterogeneity in the snowmelt, at the expense of an increase in mean bias error (0.06 to 0.22) for all distributed forcing simulations compared to the simulation with only distributed precipitation. Distributing wind speed in the energy balance calculation has a more ^{AUT:}~~complicated~~complex impact on our catchment as it accelerates snowmelt when meteorological conditions are favourable but does not generate snow patches at the end of our test case. ^{AUT:}It shows that slope and aspect based meteorological distribution can improve the spatio-temporal representation of snow cover and evapotranspiration in complex mountain terrain.

30 1 Introduction

Mountains are natural water reservoirs^{AUT:}~~, which~~ mitigate the variability of seasonal precipitation through snowpack accumulation. The gradual melting of the snowpack helps meet the demand for freshwater and energy all year long. The warmer climate expected in the near and far future for these ^{AUT:}mountain regions will impact this mitigation process.^{AUT:}~~Earth System Models~~

(ESMs) are then challenged to simulate water fluxes in mountainous catchments. Highly variable mountain topography, vegetation, soils, and geological structures affect the water transfer at different scales ^{AUT:} which makes it difficult for Earth System Models (ESM) to simulate water fluxes in mountain catchments, as they have coarser spatial scale. In particular, topography controls precipitation estimation and uncertainties related to rain/snow partition, snow redistribution, slope/aspect effect, and hill-shading that lead to spatial differences in melting (Costa et al., 2020; Fang and Pomeroy, 2020; Pomeroy et al., 2003, 2007). Fan et al. (2019) argued that variations in topography and catchment aspect can change hydrological fluxes and vegetation dynamics ^{AUT:} from steep to gentle slope and from north to south aspect in particular when comparing steep to gentle slopes or north facing to south facing slopes. Therefore, water budget modeling in the mountains is challenging, and the impacts of spatial heterogeneity, like snow depth distribution, calls for specific attention (Blöschl et al., 2019).

Land surface models (LSMs) are an imperative component of the ESMs to capture exchanges of mass, energy, and biogeochemical variables between the Earth's surface and the atmosphere (Hurrell et al., 2013; van den Hurk et al., 2011). However, hydrological flux exchange between surface and subsurface in LSMs is often poorly constrained. ^{AUT:} Major approximations include free draining subsurface hydrology and coarse resolution with no specific subgrid parameterization. The usually applied free draining subsurface approximation is not really adequate to the task. This could also include slope and aspects features (as hill shading) or meteorological subgrid variability (Clark et al., 2015; Fan et al., 2019) or underground horizontal water redistribution (Tran et al., 2020). The spatial variability of hydrological processes and associated variable flux responses are generally too fine to be represented in LSMs when used at several square km resolutions (Song et al., 2020). Bertoldi et al. (2014) mentioned that due to the lack of detailed subsurface characterization, they failed to simulate the heterogeneous soil moisture compared to observation over sloping terrains at 20 m resolution. Similarly, another study acknowledged that precipitation, solar insolation, and wind speed distribution in a hillslope catchment are vital to simulate the spatial heterogeneity in surface hydrological fluxes and snow dynamics (Sun et al., 2018). Overall, the underrepresentation of subgrid processes within mountain catchment controls the spatio-temporal snow cover, heterogeneous snow melting, and resulting streamflow responses.

^{AUT:} Differential Spatially and temporally heterogenous snowmelt in a mid-elevation catchment leads to spatial variation in saturation and pressure head response which affects streamflow at the outlet. Loritz et al. (2021) ^{AUT:} modeled a 19 km² catchment in northern Luxembourg Ardennes low elevation mountains and mentioned the importance of the distribution of rainfall data ^{AUT:} over the catchment for for the spatial representation of surface and subsurface fluxes. The same study also highlighted that in a snow dominated catchment, the calibration of hydrological models should consider the surface dynamics of snow along with ^{AUT:} the runoff runoff as evaluation variables. Furthermore, evaluating the impact of snow redistribution ^{AUT:} by the caused by wind over a catchment is challenging because it involves the hyper-resolution of wind vector (1 m to 100 m) ^{AUT:} to simulate snow transport in a mountainous catchment (Marsh et al., 2020; Pomeroy and Li, 2000). Liston et al. (2016) showed the relevance of the physical-statistical distribution of wind field in capturing snow dynamics. Similarly, shortwave radiation plays a significant role from a climatic, hydrologic, and biogeochemistry point of view. Nijssen and Lettenmaier (1999) mentioned that shortwave radiation affects the majority of ^{AUT:} energy exchanges between land and the atmosphere ^{AUT:} , including water vapor exchanges. Land surface–radiation interactions rely on terrain, wind speed, and soil moisture, and are often neglected in ESMs. Sampaio et al. (2021) highlighted that the daily/diurnal cycles of heat are also dependent on the surface orientation but are merely taken

into account in hydrological modeling. However ^{AUT:}important, forcing ^{AUT:}distribution-of-the distribution of only a single variable sometimes is not enough to capture the real catchment behaviour. Combining the terrain-based distribution of precipitation data with solar radiation and wind speed helps ^{AUT:}capturing differential snow melting to capture spatial patterns of snow melt along the slope, including distribution and redistribution of snow in the catchment (Sun et al., 2018). However, these diverse approaches in hydrological modeling are still limited and merely account for subsurface distribution, hyper-resolution simulation, terrain effect and surface meteorological variable distribution.

75 In mountainous regions, it is hard to maintain a dense network of weather stations due to the complex terrain (Meerveld et al., 2008; Revuelto et al., 2017; Song et al., 2020). This adds complexity to setting up hyper-resolution distributed models. However, there are proven statistical methods available for distributing the meteorological variables like precipitation, short-wave radiation, wind speed, temperature, and humidity over the catchment (Liston and Elder, 2006). Many studies focus only on accounting for temperature distributions in the forcings of the model to simulate the spatial variability of fluxes in snow-
80 dominated hillslope catchments (Aguayo et al., 2020; Fang and Pomeroy, 2020). However, these model resolutions remain too coarse to simulate the micro-scale hydrological behaviour. Moreover, only a few studies on snowpack simulation have used hyper-resolution distributed forcing (Günther et al., 2019; Baba et al., 2019; Vionnet et al., 2012). These studies highlighted the importance of meteorological distribution and the need for a hyper resolution modeling framework. Yet, the practice of distributing multiple meteorological forcing in hyper-resolution hydrological modeling of mountainous catchments is limited.

85 In order to overcome these LSMs limitations and quantify the impacts of fine scale variability on water balance, we ^{AUT:}studied the impact of used spatially distributed precipitation, wind speed, and shortwave radiation ^{AUT:}on the hydrological budget in a unique modeling exercise ^{AUT:}using of the hydrological budget of a small-scale alpine mid-elevation (2000-2200 m) catchment (15.28 ha) ^{AUT:}that can be investigated in details regarding surface and subsurface conditions for which we have detailed observations on surface and subsurface conditions. We ^{AUT:}have used a hyper resolution subsurface hydrological model (ParFlow) coupled with the Common
90 Land Model (CLM) at 10 m resolution to simulate the hydrological fluxes and spatio-temporal snow cover dynamics. From the perspective of hillslope hydrology we addressed the following points:

- Ability of the hyper-resolution modeling using 3D critical zone model ParFlow-CLM to capture the water/energy fluxes in a sub-alpine snow-dominated catchment.
- Impact ^{AUT:}on the catchment hydrological fluxes of distributing precipitation, solar radiation and wind speed ^{AUT:}distribution over ^{AUT:}the catchment ^{AUT:}; and its response in simulating the catchment hydrological fluxes.
- Snow cover spatio-temporal dynamics in a microscale catchment and its role in controlling the water budget.

From onward, the second section presents the study area ^{AUT:}location and its characteristics. The third section covers the methodology ^{AUT:}with details about the modeling framework. This section also includes details about the method to distribute the meteorological variables, including the modeling framework and the distribution of the meteorological variables. The fourth section details the domain
100 discretization and model setup. The fifth and sixth sections present the results and discussion, respectively. Finally, the seventh section concludes the study.

2 Study Area

2.1 Geography and geology

The study area lies in a mid-elevation ^{AUT:}~~range of sub-alpine region in the French Alps, close to the mountain pass, Col du Lautaret~~ mountain range in the southern French Alps, near the Lautaret Pass (Fig. 1). ^{AUT:}~~Being a micro-scale catchment, it~~ This micro-scale catchment covers 15.28 ha with elevation ranging between 2000 and 2200 m. It consists of steep slopes facing East in the upper area, and a wetland in the lower area. The catchment is covered by snow for 5 to 6 months per year. The warm season grassland dominates the summer with 5 % woody cover ^{AUT:}~~age~~ that includes some larches, alders and bushes. Flux'Alp meteorological station lies just ^{AUT:}~~adjacent to~~ on the border of the catchment ^{AUT:}~~(Fig. 1)~~ in a flat zone. Over the catchment, soil depths range from 110 20 cm on steep slopes to more than 2 m on the flat wetland. Soils are rich in clay with high porosity and retention capacity. This rich clay soil slowly ^{AUT:}~~transits to the hard rock towards the regolith up~~ turns into regolith, then hard rock over some transition zone, with thickness up to 5 m at the deepest locations. The base rock is highly fractured "Flysch des Aiguilles d'Arves", a shale-sandstone alternation, with bedding slopes ranging from sub-horizontal to sub-vertical (<https://infoterre.brgm.fr/>).

2.2 Climate

115 The study area is located in a typical mid-latitude alpine climate. Figure 2 shows meteorological observations for the simulated hydrological year starting on 11 November 2017 on the first snowy day to 10 November 2018. The catchment has a long winter season with 5 to 6 months of snowfall (Fig. 2a) and snow cover. Flux'Alp meteorological station records a total of 1530 mm year⁻¹ precipitation, out of which 970 mm is snow ^{AUT:}~~(dry)~~ in the studied period. According to 2017-2018 weather data, the site-average temperature is 4 °C. The site ^{AUT:}~~has below-zero winter conditions, with a~~ temperatures show a strong seasonal contrast, 120 between below-zero winter conditions (-7.4 °C ^{AUT:}minimum monthly mean ^{AUT:}in February ^{AUT:}temperature recorded) and a ^{AUT:}~~mild~~ summer (14 °C ^{AUT:}maximum monthly mean ^{AUT:}in July) ^{AUT:}temperature (Fig. 2b). ^{AUT:}~~Strong winds~~ Winds higher than 5 ms⁻¹ (Fig. 2c) are common throughout the year, usually from the South-West direction along the mountain pass (Fig. 4a). Temperature and specific humidity follow the same cyclic pattern (Fig. 2d). March is the most humid period of the year, while July is the driest. ^{AUT:}~~The studied catchment has significant differences between summer and winter solar radiation (Fig. 2f). Additionally, mountains around the catch-~~ 125 ment reduce the sunshine period with projected shadow, especially during winter Solar radiation (Fig. 2f) varies due to the seasonal cycle, and to shading effects from the southern high mountain range (elevation 3000 - 4000m elevation), which are particularly sensitive in the winter when the sun is lower on the horizon. ^{AUT:}~~These observations time series are used as the input to force the model.~~

2.3 Monitoring

Most of the monitoring on the site has started in 2012. It includes the temperature and humidity (CS215, Campbell Sc.), 130 atmospheric pressure (Setra CS100, Campbell Sc.), wind speed and wind direction (Vector anemometer A100LK and W200P, Campbell Sc.), 4 components of net radiation (CNR4, Kipp and Zonen), snow height (SR50A, Campbell Sc.), and NDVI (Normalised Difference Vegetation Index) measured through Skye Instruments SKR1800. Since 2015, the site received ^{AUT:}~~eddy~~

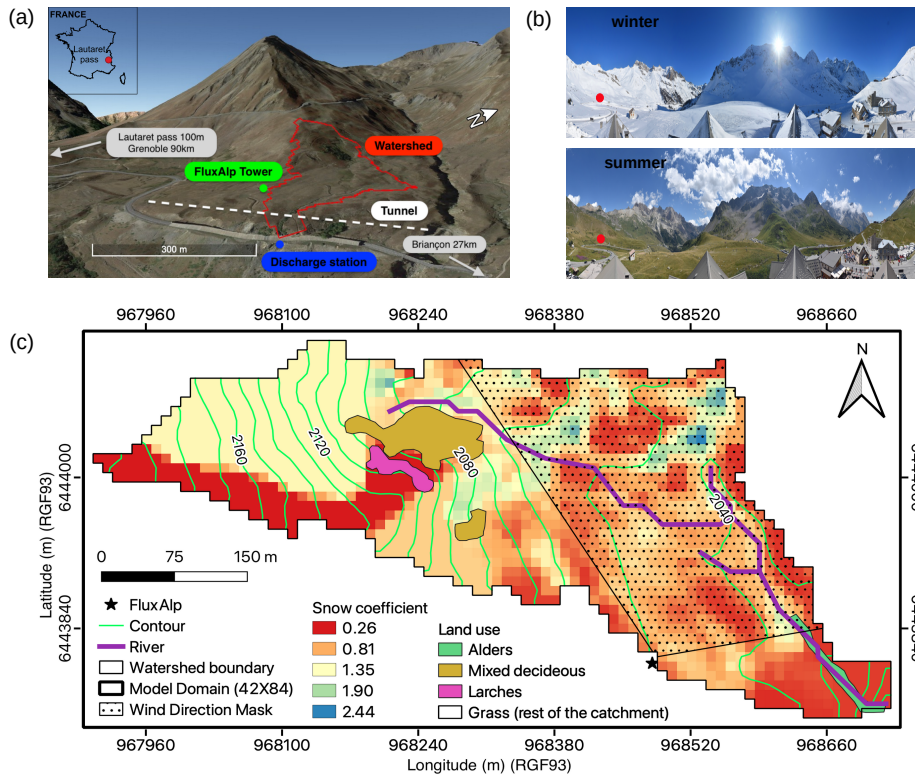


Figure 1. (a) Overview of the study area at Col du Lautaret, France, the small sub-alpine catchment is delineated in red with the outlet at the blue point. The green dot (black star in 1(c)) is the Flux'Alp micro-meteorological station. (b) Landscape views of the Lautaret pass area in winter (January) and summer (July). (c) Catchment domain (84×42 grid cells at 10 m resolution) with river branches (violet), elevation contours (green), and vegetation. Coloured pixels represent the distributed snow coefficients. The dotted area is the approximated footprint for the daily wind directions considered for ET comparison in (section 3.3).

135 eovariance-sensors one eddy covariance station composed of a LI-COR LI-7200 close-path gas analyser and a HS50 Gill 3D sonic anemometer. In 2017 an OTT Pluvio ^{AUT:}weighting rain gauge was installed at the Flux'Alp weather station. Site setup, monitoring, and data processing follow the ICOS (<https://www.icos-ri.eu/>) standards ^{AUT:}, and the site has entered in this program since 2020. All measured variables are recorded at 15 min time steps and then ^{AUT:}upscaled to a 30 min mean time series (sum for precipitation for this study) averaged over 30 min, except precipitation, which is summed. The EddyPro Software was used to process the turbulent fluxes at the same 30 min time step following the ICOS recommendations (Hellström et al., 2016).

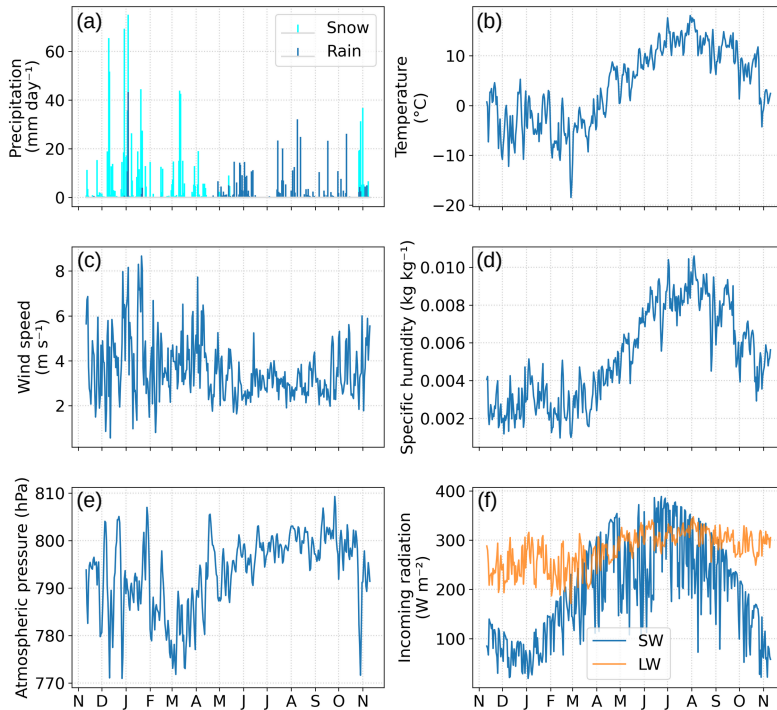


Figure 2. Daily meteorological observation at Col du Lautaret for the hydrological year 2017-2018: precipitation (a), air temperature (b), wind speed (c), specific humidity (d), Atmospheric pressure (e) and shortwave (SW) and longwave (LW) incoming radiation (f).

3 Methodology

140 3.1 ParFlow-CLM ^{AUT:}(PF-CLM)

In this study, we ^{AUT:}have used ParFlow-CLM, an integrated surface-subsurface coupled hydrological model, to simulate the impact of distributed meteorological forcing on the water transfers (Jones and Woodward, 2001; Ashby and Falgout, 1996; Kollet and Maxwell, 2006; Maxwell, 2013; Maxwell and Miller, 2005; Kollet and Maxwell, 2008). ParFlow is a parallel integrated hydrological model optimised to solve the surface and subsurface exchange of fluxes. ParFlow solves the three-
145 dimensional Richards equation to calculate the water pressure field and transfer of fluxes between unsaturated and saturated porous media (Jefferson and Maxwell, 2015). Relative permeability and soil retention curves are based on the Van Genuchten relationships (Van Genuchten, 1980). A multigrid-preconditioned conjugate gradient solver and the Newton-Krylov solver for non-linear equations (Kuffour et al., 2020) make the model efficient to run in a parallel computing environment. ParFlow includes a terrain-following grid which eases boundary conditions prescription. It accounts for the surface slope in Darcy's
150 formula, which also eases numerical exchange between subsurface and overland flow. At the model surface, excess of water ($pressure > P_{atm}$) in all saturated cell flows according to the two-dimensional kinematic wave equation (Kuffour et al., 2020). ParFlow then maintains a continuous pressure head value from the bottom to the top of the domain and explicitly calculates

fluxes between groundwater and surface water. Infiltration excess (Horton, 1933) or saturation excess (Dunne, 1983) runoff are then generated according to Richards equations. Flow-routing uses the D4 scheme to determine the flow direction based on individual slopes in the x and y direction and has been calculated according to Condon and Maxwell (2019). The CLM (Common land model) is a land surface model designed to compute the land-water-energy exchange between the Earth's surface and atmosphere (Dai et al., 2003). CLM accounts for land cover, surface temperature, soil moisture, soil texture, soil colour, root depth, leaf and stem area, roughness length, displacement height, plant physiology and thermal and optical properties of the medium to calculate the surface energy and water balance. It calculates evapotranspiration as the sum of evaporation, vegetation evaporation, transpiration, and re-condensation. ^{AUT:}~~It also includes a five adaptive layer snow scheme to predict mass of water, mass of ice, layer thickness, and temperature as main driving variables~~ CLM models snow with up to 5 layers, following layer thickness and temperature, water and ice mass in each layer. CLM two-stream radiative transfer scheme accounts for direct and scattered radiation by snow in visible and near infrared wavelengths. In CLM, when pixels cover a large range of elevation, the snow fraction is used to calculate the total snow cover area. In our study snow fraction was assigned 0 (no-snow) or 1 (snow) values. Our horizontal pixel resolution is small enough (10 × 10 m) that we consider their snow cover to be uniform. ^{AUT:}~~This implies that either our pixels are completely covered with snow or they are bare~~ This implies that our pixels are either completely covered with or completely devoid of snow. Therefore, CLM can handle the spatial/temporal snow distribution, associated water fluxes (melting, sublimation, infiltration), and evaporative fluxes according to spatial/temporal heterogeneous surface conditions (temperature, water/snow inputs, incoming radiations, wind speed, and vegetation). After computing the surface exchanges like evaporation, transpiration, snowmelt, and precipitation infiltration to and out of the soil, these are applied as source/sink in the Richards equations. Further information on ParFlow terminology and the model capability is included in the user manual (<https://github.com/parflow>).

3.2 Meteorological distribution

3.2.1 Precipitation

The precipitation data from the rain gauge ^{AUT:}~~has been~~ was first processed to account for the lack of gauge shield (Klok et al., 2001). The adopted algorithm follows as:

$$P_{corr}(x_0, y_0) = P(x_0, y_0) * (a + b * u(x_0, y_0)), \quad (1)$$

where, P_{corr} is the corrected precipitation (mm), P is measured precipitation (mm) at observation station, u is the wind speed at observation station in m s^{-1} , a and b are correction factors, and are different for rain ($a = 1.04$, $b = 0.04$) and snow ($a = 1.18$, $b = 0.20$) (Sevruk and WMO, 1986).

To account for snow cover spatial variability on the catchment domain, $S_c(x, y)$, the ^{AUT:}~~snow precipitation~~ precipitation fallen as snow at (x, y) location was calculated using a snow coefficient map $C_s(x, y)$. The snow coefficient map was prepared from the ratio between the measured snow height at the gauge to the snow height measured through the laser scan on the same day (21/02/2018) at the end of the accumulation period (Fig. 1). The snow height was calculated from the laser which ^{AUT:}~~basically~~

185 is the difference of apparent snow height (from laser scan) at the end of the accumulation period and the digital elevation
 model (DEM) for the surface without snow. The snow DEM and surface DEM were prepared at the resolution of 2 m and
 were upscaled to 10 m resolution using the ^{AUT:}~~nearest neighbour algorithm for modeling purposes~~minimum of each cell. The $S_c(x, y)$
 calculation hypothesizes that distributed snow cover on that date aggregates all spatial heterogeneity of the snow deposition
 including snow transport (redistribution). It also includes the snow compaction between the date of deposition and the laser
 190 scan. Then the corrected ^{AUT:}~~snow precipitation~~precipitation fallen as snow was calculated according to:

$$S_c(x, y) = S_m(x_0, y_0) * C_s(x, y), \quad (2)$$

where, $S_m(x, y)$ is the measured snow precipitation at the observation station. It must be noted that the laser scan didn't
 cover the upper part of the catchment. Zones not covered by the scanner were each given a fixed value according to our field
 observation. Moreover, due to the small size of the catchment and the low elevation range (1993 m to 2204 m), precipitation
 195 gradients between upper and lower elevations have not been considered and the rain has not been distributed in our study.

3.2.2 Shortwave radiation

The shortwave radiation, $SW_c(x, y)$ ^{AUT:}~~has been~~was distributed from the observed shortwave radiation measurement, $SW_m(x_0, y_0)$
 at the meteorological station considering the sun position and the terrain effect (Liston and Elder, 2006). Equation 3 partitions
 diffuse (30 %) and direct shortwave radiation (70 %) contributions from the observed shortwave radiation, and equation 4
 200 accounts for the terrain features based on their orientation which was integrated as a solar cosine function in equation 3. The
 partition of diffuse and direct shortwave radiation was taken from the CLM technical setup (Oleson et al., 2004).

$$SW_c(x, y) = (0.7 \cos i(x, y) + 0.3) * SW_m(x_0, y_0), \quad (3)$$

$$\cos i(x, y) = \cos \beta(x, y) * \cos Z(x, y) + \sin \beta(x, y) * \sin Z(x, y) * \cos(\mu(x, y) - \xi_s(x, y)), \quad (4)$$

SW_c is the corrected shortwave radiation ($W \text{ m}^{-2}$) at a coordinate location, SW_m is measured shortwave radiation at the
 205 observation station, i is the solar angle function of the slope angle β , the slope southern azimuth ξ_s , sun southern azimuth μ
 and solar zenith angle Z .

3.2.3 Wind speed

Wind speed was spatialized to better account for the estimation of turbulent fluxes (Liston and Elder, 2006). The wind speed
 was distributed as

$$210 W_w(x, y) = 1 + 0.58 \Omega_s(x, y) + 0.42 \Omega_c(x, y), \quad (5)$$

$$\Omega_s(x, y) = \beta(x, y) * \cos(\theta(x, y) - \xi(x, y)), \quad (6)$$

$$\Omega_c(x, y) = 0.25 \sum (z(x, y) - 0.5(z_i(x, y) + z_j(x, y))) / d, \quad (7)$$

$$W_c(x, y) = W_w(x, y) * W_m(x_0, y_0), \quad (8)$$

where, W_w is the wind weighting factor at a coordinate location as a function of wind direction slope (Ω_s) and curvature (Ω_c),
215 i and j are the search direction (N-S, E-W, NE-SW, SE-NW), d is 2η for cardinal axes and $2\sqrt{2}\eta$ for others, η is the search
distance and, z is the elevation, β is the slope angle, θ is the wind direction and ξ is the slope azimuth. The search distance
 d for curvature was set to 50 m (Revuelto et al., 2020). Finally, the wind weighting factor (W_w) was multiplied with the wind
speed measured (m s^{-1}) at the observation station (W_m) to obtain the terrain corrected wind speed (W_c).

220 Along with precipitation, shortwave radiation, and wind speed, three more variables are used to force the model: temperature,
pressure, and specific humidity. However, as the model was set to a microscale catchment with little elevation variability, we
did not distribute these parameters.

3.3 Wind direction mask

To compare the simulated evapotranspiration with the observation, a wind direction mask was prepared to approximately
represent the Eddy-Covariance station footprint area. ~~AUT: As we only simulate a small catchment, actual footprint is sometimes not included in
the limits of the catchment. To overcome this problem we have~~ As the catchment and the footprint area only partly coincide, we
225 selected simulated pixels in an approximated footprint area based on a wind direction mask (Fig. 1) and averaged simulated values
over the mask. The wind direction mask was prepared according to the prevailing wind directions towards the Flux'Alp station
between the 10 percentile (122.39°) and 90 percentile (260.51°) wind direction. ~~AUT: We assumed that when the wind blows towards this
direction there is an enhanced similarity between observed and simulated evapotranspiration.~~ We then compared observed evapotranspiration to
230 the simulated average value over the mask, only when the wind blows from a direction included in the mask, as this maximises
the comparability of simulated and measured values.

3.4 Sentinel-2 snow cover

Snowmelt dynamics was compared to Sentinel-2A and Sentinel-2B products from Sentinel-2 mission developed by European
Space Agency (ESA) for high resolution satellite imagery (Drusch et al., 2012). We ~~AUT: have~~ downloaded four Sentinel-2 images
235 out of which two belong to the accumulation period and two ~~AUT: belong~~ to the melting period. These images were selected to
show the spatial and temporal distribution of snow in the catchment. For this purpose, we have calculated the normalised snow
difference index (NDSI) from the downloaded images as (Dozier, 1989),

$$NDSI = \frac{Green(band3) - SWIR(band11)}{Green(band3) + SWIR(band11)}, \quad (9)$$

where, 'Green' and 'SWIR' are the corresponding bands in the green and shortwave infrared region of the satellite, respectively.
240 The green band is represented by 'band 3' and the SWIR band is represented by 'band 11' in Sentinel-2 product. ~~AUT: Sentinel~~
'band 3' was available at 10 m resolution while 'band 11' at 20 m resolution. NDSI calculation was carried out by resampling
'band 11' at 10 m resolution (Hofmeister et al., 2022). The Sentinel-2 snow pixels were selected with $NDSI > 0.4$ (Riggs et al.,
1994). In the model, the snow pixels were selected for snow depth threshold over 1 cm ~~AUT: ,~~ which is the minimum non zero
height for snow.

245 ~~AUT: [New section on 'Performance indicators' added below.]~~

3.5 Performance indicators

3.5.1 Slope

Slope for the linear regression without intercept ($y = \alpha x$) is represented as,

$$\alpha = \frac{\sum_{i=1}^n (x_i y_i)}{\sum_{i=1}^n (x_i^2)}, \quad (10)$$

250 where, x is observed value and y is predicted value.

3.5.2 R-square (R^2)

R-square or coefficient of determination is defined as,

$$\left[\frac{\sum_{i=1}^n (x_i - \bar{x})(y_i - \bar{y})}{\sqrt{\sum_{i=1}^n (x_i - \bar{x})^2} \sqrt{\sum_{i=1}^n (y_i - \bar{y})^2}} \right]^2, \quad (11)$$

where, x is the observed value and y is the predicted value, and \bar{x} , \bar{y} are the mean of observed and predicted values, respectively.

255 3.6 Root mean square error (RMSE)

RMSE score is represented as,

$$\sqrt{\frac{1}{n} \sum_{i=1}^n (x_i - y_i)^2}, \quad (12)$$

where, n is the number of samples and x is observed value while y is predicted value.

3.7 Mean bias error (MBE)

260 MBE score is represented as,

$$\sqrt{\frac{1}{n} \sum_{i=1}^n (y_i - x_i)}, \quad (13)$$

where, n is the number of samples and y is predicted value while x is observed value. MBE score is represented for the Sentinel-2 images as an average between the spatial similarity of snow and non-snow pixels (mismatch between the image pixels).

265 4 Domain discretization and simulation setup

The surface domain of 15.28 ha was discretized at a ^{AUT}horizontal hyper-resolution of 10 m with the total number of $84 \times 42 \times 11$ (longitude \times latitude \times levels) cells on a terrain following grid (Fig. 1). ^{AUT}Individual cell height (z-direction levels) varies

from 4 cm for the top soil layer to 110 m for the deepest layer (Fig. 3a). ^{AUT:}As mentioned earlier, the model was mainly built and forced using the observations; hence, the input data either belongs to observation data or ^{AUT:}secondary data derived from observation. These data include ^{AUT:}the temperature, precipitation, wind speed, short wave, humidity, and atmospheric pressure plotted in figure 2. ^{AUT:}These observations data were available at 30 minutes intervals from the instruments. The data which were available at a higher temporal resolution were upscaled to the 30 minutes temporal resolution using the mean and sum approach. Leaf Area Index (LAI) ^{AUT:}and Stem Area Index (SAI) ^{AUT:}were was calculated from NDVI measurements ^{AUT:}while Stem Area Index (SAI) was assigned a constant value based on field survey. Displacement height (d) and roughness length (z0) were calculated from the vegetation height following Brutsaert rules (Brutsaert, 1982). ^{AUT:}Grass height was calculated from the snow height sensor during the summer months considering NDVI to identify the vegetation/snow periods. The snow height sensor show sensitivity to the grass height when there was no more snow on the ground. We, therefore, used the signal of this sensor when NDVI values were above 0.4 to estimate grass height. LiDAR Digital Surface Model (DSM) of 2 m resolution was available for the catchment and upscaled to 10 m resolution ^{AUT:}for various elevation related parametrization in the model using the minimum of each cell. Upscaled DSM ^{AUT:}has been was processed with PriorityFLOW to generate the slope maps in x and y direction (Condon and Maxwell, 2019). The Landcover map was made through field observations while the Manning coefficients were assigned using the landcover map. ^{AUT:}River pixels were assigned a constant manning value of $0.05 \text{ s m}^{-1/3}$ and the rest of the catchment were assigned a constant manning value of $0.03 \text{ s m}^{-1/3}$. The lateral and bottom boundary conditions were set to no flow and the surface boundary condition was ^{AUT:}set at atmospheric pressure ^{AUT:}condition that allows ^{AUT:}surface runoff fluxes to leave at positive hydraulic head (Kollet and Maxwell, 2006). Hence, the inflow and outflow were restricted to exchange only through the surface. Subsurface ^{AUT:}has been was made heterogeneous with three layers consisting of soil, regolith, and flysch ^{AUT:}which were divided into 11 numerical cells with a total of 11 different layers (Fig. 3a). The bottom of the domain was set deep enough to accommodate various subsurface water transfers (118 m deep from the surface). The soil physical parameters used in this study include porosity, permeability, soil horizons, and Van Genuchten parameters. The ^{AUT:}resulting water retention curves ^{AUT:}are were plotted on Fig. 3c, d for the three different horizons. They show a reduction of permeability and porosity with depth. Soil horizons distribution (Fig. 3b) was determined from an electromagnetic survey measuring apparent electrical conductivity (related to water and clay content) and ground penetrating radar (GPR) measuring soil thickness. Electromagnetic survey ^{AUT:}has been was done for the whole catchment however, GPR survey ^{AUT:}has been was performed for three transverse profiles across the stream to validate the electromagnetic survey. The soil properties were determined by field permeability experiments and laboratory mercury porosity experiments. Elaboration about the detailed hydro-geological characterization is beyond the scope of this study and will be detailed in a companion paper (Gupta et al., 2022, in preparation). This study is more focused on surface dynamics due to ^{AUT:}surface meteorological variable distribution.

The model ^{AUT:}has been was forced with half-hourly meteorological forcing, however, results were ^{AUT:}written saved at hourly time-step. The Universal Time Zone (UTC) was considered in terms of monitoring and modeling for this study. Before running the actual simulations, a 10-year spin-up ^{AUT:}run ^{AUT:}was performed with ‘SeepageFace’ (no runoff) conditions ^{AUT:}was performed to bring the model into a hydrological balance. The yearly subsurface storage difference ^{AUT:}is used as spin-up parameter which reached the equilibrium was used to evaluate whether the spin-up had taken the model into equilibrium, which happened at the end of

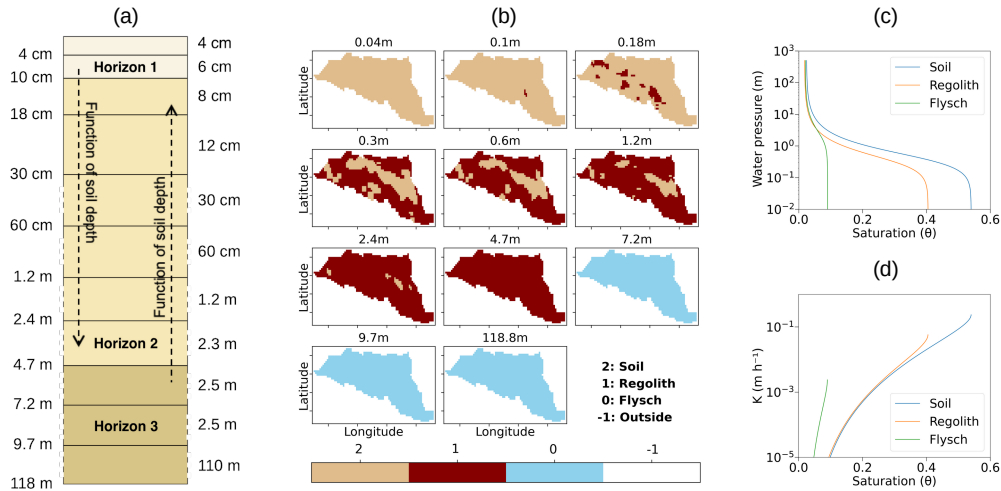


Figure 3. Subsurface configuration used for discretizing the domain. (a) The vertical distribution of the subsurface layer with the thickness (right) and depth (left) of each grid cell. (b) Spatial distribution of subsurface layer including soil (burly wood), regolith (dark brown), and flysch (blue). These layers vary in their hydro-geological parameters e.g. in terms of conductivity, and porosity to the soil transfer functions which are shown in (c- Soil retention curve) and (d- hydraulic conductivity curve).

the 10th year. AUT: Each simulation was also run for two consecutive years with the same forcing to avoid any imbalance in subsurface storage (Ajami et al., 2014). The different simulations setup for this study AUT: include are detailed in table 1.

305 AUT: 1-dimensional column simulation of only precipitation distributed mean forcing (1D-PM)

AUT: 3-dimensional simulation of only precipitation distributed mean forcing (1D-PM)

AUT: 3-dimensional simulation of all distributed mean forcing (1D-AM)

AUT: 3-dimensional simulation of all distributed forcing (2D-AD)

AUT: 3-dimensional simulation of only precipitation distributed forcing (2D-PD)

310 AUT: 3-dimensional simulation of only shortwave radiation distributed forcing (2D-SD)

AUT: 3-dimensional simulation of only wind speed distributed forcing (2D-WD)

All simulations named 1D AUT: are the simulations with non distributed forcing use forcings that are uniform across the watershed (Table 1). Rain is the major hydrological model input hence, we keep the same amount of precipitation input in all simulations (1443.72 mm), which corresponds to the spatial average of precipitation after applying the distribution AUT: formulae correction (eq. 2). Precipitation is reduced compared to what is measured at the rain gauge station (1531.96 mm) because the precipitation distribution process leads to a non-conservative spatial snow distribution over the catchment. AUT: This The equal amount of precipitation input leads us to easily see the partitioning between different hydrological fluxes AUT: among separate across the different meteorological forcing simulations. AUT: 1D-PM, therefore, corresponds to a classical hydrological simulation for a small catchment when one applies the meteorological forcing directly from a nearby weather station. By contrast, 1D-AM accounts for
 320 local terrain slope and aspect according to equation 5-8, and applies uniformly across the watershed the mean corrected in-

coming radiation. ^{AUT:} Similarly, Therefore, shortwave radiation amount is not the same considering the measured value (^{AUT:} yearly averaged shortwave radiation ^{AUT:}, 1D-AM: 190.8 W m^{-2}) and the ^{AUT:} mean distributed value ^{AUT:} (yearly averaged shortwave radiation, 1D-PM: ^{AUT:} 152.1 W m^{-2}) ^{AUT:} when taking into account the slope angles ^{AUT:} (152.1 W m^{-2}) ^{AUT:}. The shortwave radiation distribution scheme accounts for the slope hence, the shortwave radiation on average is reduced: as the weather station is less shaded than the generally east facing watershed, accounting for slope and aspects reduces the average incoming radiation. ^{AUT:} Meteorological parameters were further distributed to better analyse their respective influence. Pix-PM, 2D-PD, and 2D-WD all relate to 1D-PM, and used the zenithal solar radiation observation (measured shortwave radiation) directly from the radiation sensor ^{AUT:} For shortwave radiation forcing, we did several simulations to better analyse the results. Pix-PM, 1D-PM, 2D-PD, and 2D-WD are run with the zenithal solar radiation observation (measured shortwave radiation) directly from the radiation sensor. ^{AUT:} 2D-AD and 2D-SD are related to 1D-AM as they used the same distributed incoming solar radiation, according to equation 5-8. ^{AUT:} and 2D-AD and 2D-SD are run with distributed solar radiation according to equations 5-8. The average of the distributed shortwave radiation is used to force the 1D-AM simulation (Table 1). 1D-PM corresponds to a classical hydrological simulation for a small catchment when one applies the meteorological forcing directly from a nearby weather station. The latter four proposed simulations ^{AUT:} have been were run to quantify the effect of spatially distributed forcing all together or individually ^{AUT:} (Table 1).

^{AUT:} Meteorological distribution algorithms described in section 3.2 aims at representing the slope, curvature, and aspect effect in the spatial distribution. Meteorological forcings were distributed according to algorithms described in section 3.2. to represent the effects of slope, curvature and aspect on the spatial distribution of those forcings. Fig. 4 presents snapshots of heterogeneities produced by these algorithms. Even at a micro-scale, one can observe the spatial meteorological variability along the grid after applying equations 2-8. In Fig. 4b, for an averaged 0.53 mm snow rate, the distribution algorithm produce ^{AUT:} s large heterogeneities ranging from 0.2 mm to 1.2 mm ^{AUT:}. Deeper accumulation is, with deeper accumulation mainly on lowlands. Similarly for shortwave radiation (Fig. 4c) for input radiation of 400.8 W m^{-2} on November 11 at noon, the algorithm ^{AUT:} reduces reduced the radiation to 349.7 W m^{-2} on average with more than (+/-) 50 W m^{-2} ^{AUT:} difference depending on the location. In wind speed distribution, there ^{AUT:} is was not so much variation in the spatial mean before and after wind speed distribution. The mean wind speed before and after the spatial distribution ^{AUT:} is was 5.6 m s^{-1} and 5 m s^{-1} , respectively (Fig. 4d).

345 5 Results

5.1 ^{AUT:} Non-distributed forcing simulation Simulations with spatially uniform forcings

^{AUT:} 1D-PM and 1D-AM represent our reference simulations, with uniform forcings across the watershed (see Table 1). Their results were presented in Figure 5. ^{AUT:} Figure 5a, b shows the catchment response from According to the 1D-PM ^{AUT:} simulation ^{AUT:} (Fig. 5a) ^{AUT:} for a full hydrological year and the monthly budgets for storage variation, surface and subsurface fluxes. It shows that the hydrological year begins with the snow accumulation period until the end of March. December and January ^{AUT:} are were the snowiest ^{AUT:} months pe-riods ^{AUT:}. Some, with some snowmelt events (magenta line) ^{AUT:} that can be observed during this period because of due to short above zero degree episodes ^{AUT:} (Fig. 2b) ^{AUT:} but, which generate very little runoff (black line). In April, ^{AUT:} warmer positive temperatures and rain on snow events generate continuous melting ^{AUT:} in our simulation and ^{AUT:} is simulated because of warmer positive temperature (Fig. 2b)

Simulation ID	Precipitation	Shortwave radiation	Wind speed	Description
Pix-PM	Distributed mean	Non-distributed	Non-distributed	1-D column simulation with only precipitation distributed mean forcing
1D-PM	Distributed mean	Non-distributed	Non-distributed	3-D simulation of only precipitation distributed mean forcing
1D-AM	Distributed mean	Distributed mean	Distributed mean	3-D simulation of all distributed mean forcing
2D-WD	Distributed mean	Non-distributed	Distributed	3-D simulation of only wind speed distributed forcing
2D-SD	Distributed mean	Distributed	Non-distributed	3-D simulation of only shortwave radiation distributed forcing
2D-PD	Distributed	Non-distributed	Non-distributed	3-D simulation of only precipitation distributed forcing
2D-AD	Distributed	Distributed	Distributed	3-D simulation of all distributed forcing

Table 1. Distributed and non-distributed approach adopted for different simulations.

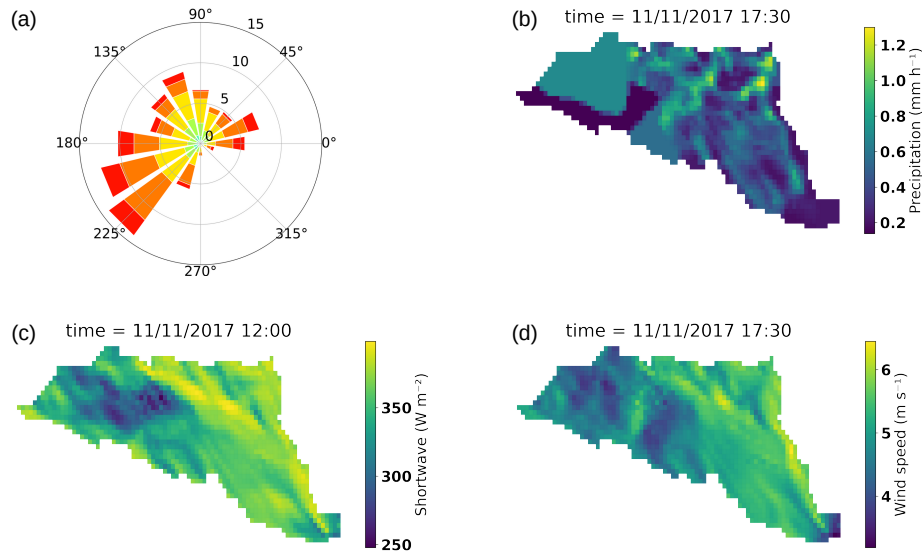


Figure 4. (a) Windrose diagram. (b) Precipitation distribution along the catchment. (c) Shortwave radiation distribution over the catchment. (d) Wind speed distribution over the catchment. All are plotted for the 11/11/2017 at 5:30 pm and 12:00 pm for shortwave radiation.

355 but also rain on snow events. This produce^{AUT}s the highest river discharge peaks ^{AUT} on the hydrograph which follows the with a strong daily cycle^{AUT}: (between min and max discharge values at daily timestep) and the rain timing (highest discharge peaks), further intensified by coinciding

rain events. This period also increase^{AUT:sd} the subsurface storage^{AUT:(Fig-5b)} which produce^{AUT:s} a base flow^{AUT:that combines} with the snowmelt contribution to the streamflow later in May (Fig. 5b).^{AUT:} In May streamflow show a combination of base flow and snowmelt (snowmelt in May in Fig. 5a, subsurface storage decrease in May in Fig. 5b).

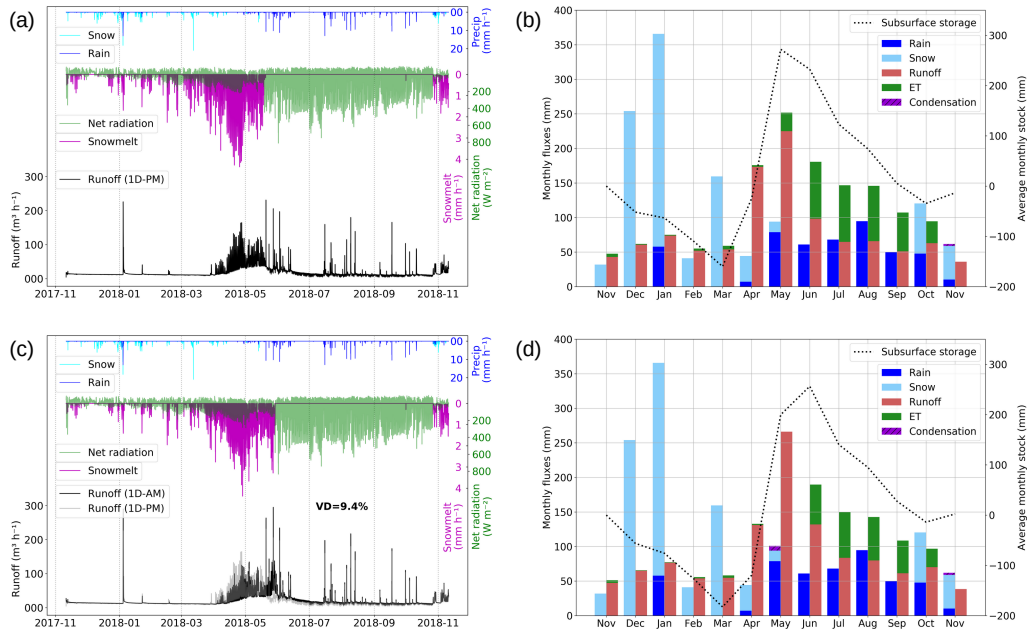


Figure 5. (a) Precipitation (rain – blue and snow – light blue), streamflow (black), snowmelt (magenta) and net radiation (green) regimes along the simulation period for only precipitation distributed mean simulation (1D-PM). (b) Monthly water budget for 1D-PM simulation including rain (blue) snow (light blue), Runoff (red), ET (green), and condensation (purple). The Black dotted line is the total subsurface water storage. (c)(d) same as (a) and (b) but for all distributed mean simulation (1D-AM). VD is the volume difference in percentage between plotted simulations.

One of the most important and noticeable point^{AUT:s} while using^{AUT:the non-distributed forcing} ^{AUT:iswas} the sudden disappearance of the snow at the end of the snowmelt season, which^{AUT:is usually not observed} ^{AUT:on actual in the field.} ^{AUT:ThisIt} means that all the pixels behaved in the same way^{AUT:;} and there^{AUT:iswas} no noticeable impact on the ^{AUT:subsurface hydrology of the catchment} spatial snow variability when considering a uniform forcing. From June to the beginning of the next snow period, summer rain produce^{AUT:s} almost instantaneous river response^{AUT:s} and subsurface storage sustain^{AUT:s} stream ^{AUT:discharge} runoff for several months. During this period, one can note a radical change of net radiation because of the ^{AUT:change of the albedo} ^{AUT:land cover change} from snow ^{AUT:cover to herbaceous to grass.} The net radiation contributes to snowmelt in early spring. Factors responsible for this phenomenon include^{AUT:s} higher sun elevation, clear sky conditions, and higher daily temperature.

During winter and spring^{AUT:;} the monthly cumulated ET ^{AUT:iswas} very small (Fig 5b) because of low available energy and complete snow cover^{AUT:age}. After the complete snowmelt, the model simulate^{AUT:sd} much higher monthly cumulated ET ^{AUT:ae-} ^{AUT:according to the prescribed} following the LAI cycle. ET at this period ^{AUT:iswas} higher than the monthly cumulated rain (June, July,

370 September), which means that ET participates in the extraction of shallow water storage during the summer. This can be seen by the difference in subsurface storage decline between the summer (higher water storage diminution) and the winter (lower water storage diminution). In October one can notice a small increase in ^{AUT:}the subsurface storage when ET decreases because of vegetation decay. At the end of the hydrological year, the subsurface water storage has a deficit of ^{AUT:}0.15-0.62 mm, which is much smaller than the annual cycle amplitude.

375 ^{AUT:}Figure 5c, d present the same time series and monthly water budgets for the 1D-AM simulation. ^{AUT:}1D-AM simulation (Fig. 5c, d) mostly differs from 1D-PM ^{AUT:}The major difference ^{AUT:}compared to 5a, b ^{AUT:}is that as precipitation, solar radiation and wind velocity ^{AUT:}are were prescribed using the spatial average of the distributed ^{AUT:}field forcing. ^{AUT:}The ^{AUT:}This ^{AUT:}major difference comes from solar radiation reduction ^{AUT:}reduces solar radiation from 190.8 W m⁻² to 152.1 W m⁻² on average which reduces melting and ET. ^{AUT:}Snow lasts 9 more days on the ground, runoff increases from 73% to 80% of total precipitation (runoff coefficient, Table 2), and infiltration ^{AUT:}increases by 10.66 mm ^{AUT:}It leads to a 9 days longer snow period, an increased runoff and an increased infiltration of 34.61 mm (Table 2). ^{AUT:}This unbalance vanishes after 10 years leading to a higher water table and then higher runoff with a 0.8 runoff coefficient when a steady state is reached. ^{AUT:}This means that ~~f~~For similar geomorphology, any reduction in input solar radiation because of catchment orientation or else ^{AUT:}will lead ^{AUT:}leads to higher water tables and then higher runoff coefficient. ^{AUT:}Compared to the 1D-PM simulation this simulation showed reduced runoff peaks in the early melt season which leads to more percolation. Increased percolation leads to higher ^{AUT:}base flow during the late summer and delays the base flow response by around one month compared to 1D-PM simulation. ^{AUT:}Runoff in the 1D-AM simulation increases overall by 9.4 % compared to the 1D-PM simulation.

5.2 ^{AUT:}Distributed forcing simulations Simulations with spatially distributed forcing

^{AUT:}In the following section, we will discuss the differences in surface hydrological fluxes for all combined and individually distributed simulations, along with their role in streamflow generation.

390 ^{AUT:}This section present the simulation run with a fully distributed forcing (2D-AD), with its difference from the previous uniformly forced simulations, and the three simulations based on forcings with only one distributed variable (2D-WD, 2D-PD, 2D-SD) to explore the contributions of each individual spatial distribution. ^{AUT:}Looking at the surface fluxes on Figure 6a ^{AUT:}, one can see that ^{AUT:}show that snowmelt lasts longer in 2D-AD simulation, tailing across June and early July, with streamflow decreasing until even later in July ^{AUT:}the simulation with all distributed forcing (2D-AD) have longer snowmelt period with a long steady decline during the ^{AUT:}streamflow recession till mid-July. ^{AUT:}These snowmelt dynamics were smoother than it was simulated in either uniformly forced simulation (1D-PM and 1D-AM) ^{AUT:}Compared to the non-distributed forcing simulation 1D-PM, the distributed forcing is causing a smoother snowmelt dynamic ^{AUT:}which last till July and correspondingly impacts the net radiation, recharge and streamflow discharge dynamic. ^{AUT:}In the most intense melt period in May, this resulted in ~30% lower peak streamflow values in 2D-AD compared to 1D-AM or ^{AUT:}1D-PM simulations. ^{AUT:}It leads to significant differences for streamflow values during the core of the melting period up to 50 % more for 1D-AM and ^{AUT:}1D-PM compared to 2D-AD. However, ^{AUT:}the resulting annual water budget ^{AUT:}terms ^{AUT:}have changed only ^{AUT:}by 2 % ^{AUT:}difference at ^{AUT:}scale of annual water budget between 1D-AM and 2D-AD simulations ^{AUT:}, and by -7 % between 1D-PM and 2D-AD simulations. ^{AUT:}As mentioned in the previous section, time averaged distributed shortwave radiation input was lower in simulation 1D-AM compared to 1D-PM, due to accounting for shading effects. Simulation 2D-AD has the same time average radiation input as

405 1D-AM and was closer to this simulation in the yearly budget. ^{AUT:}From this point of view, forcing distribution at that scale seems not to add much information compared to a 1D forcing. Small scale distribution of meteorological forcings therefore only adds information on dynamics, and not on yearly budgets. ^{AUT:}1D-AM simulation has a mean of distributed shortwave which reduces the surface runoff from snow melt and more percolation to the subsurface. This percolation appears as base flow in late summer which becomes very close to the runoff volume of 2D-AD simulation. ^{AUT:}The tailing snowmelt through June generated more percolation to the subsurface, resulting in stronger base flow in late summer, thereby catching up with the total runoff volume simulated in 1D-AM.

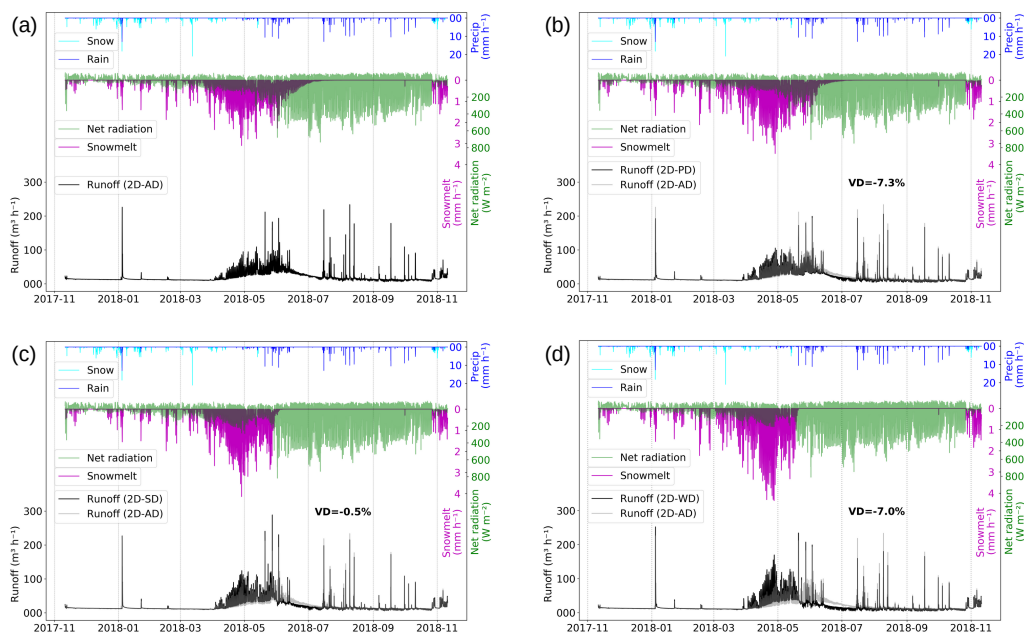


Figure 6. Same figure as 5a for (a) all distributed run (2D-AD), (b) only precipitation distributed run (2D-PD), (c) only shortwave radiation distributed run (2D-SD) and (d) only wind speed distributed run (2D-WD). VD is the volume difference in percentage between plotted simulation.

410 ^{AUT:}Looking at As visible in the results of the simulations with only one distributed forcing ^{AUT:}individually distributed simulations ^{AUT:}results (Fig. 6b, c, d), ^{AUT:}it seems that the ^{AUT:}this smoothing effects smoother decline in snowmelt ^{AUT:}is caused by resulted from both the precipitation and shortwave radiation distribution ^{AUT:}(Fig. 6b, c). ^{AUT:}At the contrary However, the simulation 2D-WD, where only the wind speed forcing was distributed, did not present such a smooth decline on snowmelt and ^{AUT:}only wind speed distributed (2D-WD) results ^{AUT:}seem were very similar to the non-distributed ^{AUT:}results simulation (1D-PM). ^{AUT:}One can even refer to figure 6d for easier inter-comparison with figure 5a. The melting period tail length ^{AUT:}seems to be was controlled by the snowpack depth variability (Fig. 9a, b) and higher accumulated snow on some pixels. This ^{AUT:}is combined combines with solar radiation effects, which also produce ^{AUT:}s spatial variability in snowmelt on the catchment even if the snow precipitation ^{AUT:}is was uniformly distributed (Fig. 6c). Only wind speed distribution (2D-WD) simulation ^{AUT:}shows showed the highest melting regimes from mid-March to mid-May when temperature and incoming radiations ^{AUT:}are were favourable for melting ^{AUT:}with resulting in daily melting peaks

420 larger than 4 mm h^{-1} (Fig. 6d). In detail, wind speed distribution show^{AUT:s} ^{AUT:}an increase in the melting rate which leads to higher subsurface storage when compared to 1D-PM.

Streamflow differences between simulations basically follow the melting differences. The impact of the late April and early May rain-on-snow period ^{AUT:iswas} visible on streamflow on figure 6a, b. It must be noted that ^{AUT:there are differences in term of incoming solar radiation}incoming solar radiation differ between simulations. ^{AUT:Due to non-distributed shortwave radiation in}
425 ^{2D-PD simulation, the melting peaks were higher compared to 2D-AD simulation. This resulted in rapid runoff in 2D-PD simulation and less percolation to subsurface which caused a volume difference of -7.3 % compared to 2D-AD simulation.}
^{AUT:UnsurprisinglyThe} 2D-WD and 2D-PD simulations showed ^{AUT:larger}lower streamflow values compared to 2D-AD and 2D-SD simulations. This happen^{AUT:sed} because for the former two, the catchment receives 38.7 W m^{-2} less radiation than the latter two. ^{AUT:The shortwave radiation distribution slowed the melting, which enhanced percolation to the subsurface. This subsur-}
430 ^{face percolation appeared as the base flow in the late summer. Though the base flow in 2D-SD simulation was lower than 2D-AD, however, due to equal precipitation in all pixels, 2D-SD simulation showed higher early melting peaks (Fig. 6c). This counter balance between 2D-AD and 2D-SD simulation showed a volume difference of only -0.5 %. In 2D-WD simulation due to rapid runoff at melting season, the subsurface storage decreased which result in far lower baseflow with volume difference of -7.0 % compared to 2D-AD simulation (Fig. 6d). To conclude, the amount of precipitation in a pixel correlated with the}
435 ^{snowmelt peaks; however, rapid melting decreases the subsurface storage which result in lowered streamflow. Concerning the}
^{AUT:late} summer period when snow gets melted, these differences ^{AUT:areWERE} not visible on the streamflow.

^{AUT:Figure 7 shows observed and simulated evapotranspiration time series over the two weeks summer window from 08/07 to 25/07 and scatter plots over the two vegetative months from early July to end of August. This is a snow free period. For better comparison with observations we selected simulated pixels in an approximated footprint area based on a wind direction mask (Fig. 1) and averaged simulated values over the mask (section 3.3).} ^{AUT:Pixel simulation}
440 ^{(Pix-PM) corresponds to the 1D vertical column run at FluxAlp cell (without lateral flow).}

^{AUT:The}Evapotranspiration in the pixel run (orange curve and orange dots) ^{AUT:was} clearly overestimated ^{AUT:compared to} observed evapotranspiration as one can see on both the time series and the scatter plots. ^{AUT:This is also the case}Similarly^{AUT:}, ^{AUT:for} the non-distributed simulation (green curve and green dots^{AUT:}, 1D-PM)^{AUT:}, ^{AUT:and for}and the distributed simulations 2D-PD and 2D-WD ^{AUT:which} have comparable evapotranspiration amplitude (Fig. 7c, e). However, 2D-AD and 2D-SD ^{AUT:have}show
445 reduced simulated ET which better matches the observations (Fig. 7b, d). This ^{AUT:happens because the average shortwave radiation after the distribution is less than the shortwave radiation without distribution (section 4). Also, the catchment is facing east which actually reduces direct incoming solar radiation from noon to sunset}reflects the lower (average) shortwave radiation in the forcings where the solar radiation has been distributed according to the terrain (section 4): as the catchment generally faces east, this distribution reduced the direct
^{incoming solar radiation from noon to sunset.}

450 The evapotranspiration ^{AUT:ofin} both Pix-PM and 1D-PM overestimate^{AUT:sd} ET compared to observations. First the pixel run (Pix-PM) ^{AUT:iswas} supposed to simulate a catchment border (Flux'Alp location) with dryer soil/ground condition (top of a ridge) and the ET observations ^{AUT:arewere} supposed to average both the wet zone^{AUT:s} close to the river and the dryer zones. However, it ^{AUT:iswas} not the case in our ^{AUT:pixel}2D-AD and ^{AUT:1D-PM}2D-SD simulations. ^{AUT:The linear slope in these two simulations moved much close to the identity line (slope = 1.18) compared to other simulations. This explains that along with}

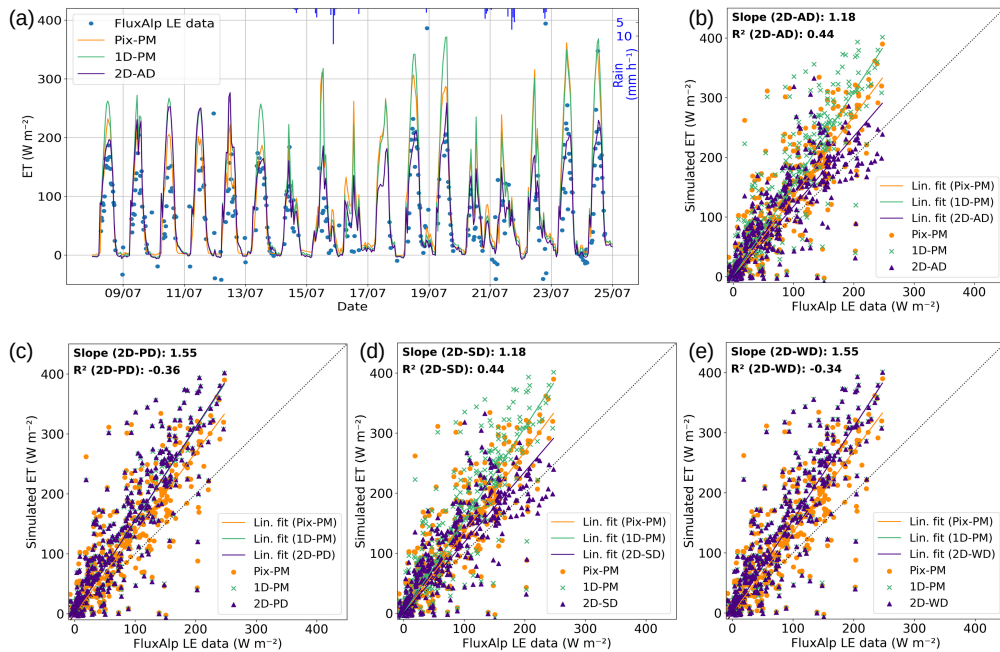


Figure 7. (a) Evapotranspiration simulation masked with wind direction mask for 17 days in summer for all distributed run (2D-AD). Scatter plot for the July-August 2018 period for (b) all distributed run (2D-AD), (c) only precipitation distributed run (2D-PD), (d) only shortwave radiation distributed run (2D-SD) and (e) only wind speed distributed run (2D-WD). The slope line represents the corresponding linear fit for the scatter plots, slope value of each simulation highlighted at the top.

455 subsurface percolation, the shortwave radiation distribution simulated the better ET. In 2D-PD and 2D-WD simulations, the
 460 linear slope equals the slope of the pixel run (slope = 1.55) which corresponds to much higher evapotranspiration compared to
 observation. Shortwave radiation distribution (Fig. 7d) ^{AUT:}seems to have showed the most important impact in our measurement
 area. ^{AUT:}Shortwave radiation distribution showed the smoothed runoff curve, higher subsurface percolation, increased base flow
 and increased runoff. The corresponding reduced ET in 2D-SD (and 2D-AD), averaged on the footprint area, also corresponds
 460 much better to the ^{AUT:}Eddy Covariance observations ^{AUT:}(decrease in regression slope from 1.55 to 1.18).

5.3 Hydrological budget

Annual water budgets (Table 2) show ^{AUT:}s that the ^{AUT:}main impact of forcing distribution is caused by the shortwave radiation distribution
 and subsequent ET calculation ^{AUT:}has large impact. It made a difference of ~100 mm at the annual budget scale. This increases
^{AUT:}the runoff coefficient from 0.73 to 0.77 runoff from 73% to 79% of the total annual precipitation ^{AUT:}by diverting the difference of
 465 flux towards runoff. ^{AUT:}One can also note This also result in the water storage change over the year ^{AUT:}as explained in previous sec-
 tion. As we started from the same initial conditions for all simulations ^{AUT:}and additionally run the spinup for another 2 years,
 it ^{AUT:}reaches reached more than ^{AUT:}30 10 mm ^{AUT:}in subsurface storage when SW is reduced (1D-AM, 2D-AD and 2D-SD) and

Simulations	Precipitation (mm)	Runoff (mm)	Runof coef. ^{AUT:(mm)}	ET (mm)	Subsurface storage (mm)
1D-PM	1443.72	1060.74	0.73	372.94	-0.62
1D-AM	1443.72	1159.99	0.80	263.30	10.66
2D-AD	1443.72	1142.30	0.79	266.78	11.68
2D-PD	1443.72	1058.87	0.73	361.48	-0.78
2D-SD	1443.72	1136.39	0.79	269.71	14.98
2D-WD	1443.72	1062.48	0.74	372.23	5.96

Table 2. Annual water budget terms in the catchment for different simulations.

^{AUT:45.5}5.96 mm for 2D-WD simulation. ^{AUT:4}The subsurface storage change remains ^{AUT:much} much smaller than the ET difference and ^{AUT:it minimizes}doesn't impact the runoff coefficient ^{AUT:hence not change our conclusions}.

470 Figure 8 shows monthly water budgets for 2D-AD and individually distributed simulations. Snow precipitation from November to March ^{AUT:does not}do not infiltrate much to fill up the subsurface storage (dotted line). January rain on snow events slightly reduce the subsurface storage. Very similar runoff values ^{AUT:are were} observed ^{AUT:up to the end of February} among the different ^{AUT:forcing scenarios}scenarios. In contrast, from mid ^{AUT:-} March to June the subsurface storage ^{AUT:is was}replenished by melting (^{AUT:Fig. 5a, Fig. 6}) ^{AUT:and runoff increases}which later increases the runoff. The 2D-WD forcing produced the largest values of recharge 475 (~430 mm) and the ^{AUT:2D-SD}2D-AD the largest values of streamflow. From May to October, streamflow at the outlet and ET decrease ^{AUT:sd} the subsurface storage. Higher shortwave radiations (2D-PD and 2D-WD) led to longer ET periods. One can finally note that reduction in ET because of vegetation senescence in November ^{AUT:leads to increased and beginning of}subsurface storage.

5.4 Snow dynamics

480 Figure 9 shows the temporal dynamics of the snow ^{AUT:mantle}mantle and the impact ^{AUT:in terms of}On albedo. Snow depth plots for Pix-PM run (purple line) and 1D-PM run (red line) ^{AUT:are were}superimposed. The 1D-PM run show ^{AUT:s} little variability in snow depth (red shading). ^{AUT:These two run follow a dynamic consistent with the observations (black line) and an overestimation along the accumulation period}The ^{AUT:dynamics of these two runs is consistent with the observations (black line) although snow height is overestimated during the initial accumulation period.} ^{AUT:This is}This was probably because of the rough snow/rain partition temperature threshold and the 485 inability of the snow scheme to account for compaction. The snowmelt dynamic ^{AUT:is}is particularly well simulated (snow cover within the Sentinel-2 image acquisition date), especially along the dry period at the end of April. In early May one can note some discrepancies again probably because of our limited ability to separate rain and snow in the precipitation forcing, close to the phase change temperature ^{AUT:range}range. This can be seen on the pixel simulated ^{AUT:A}albedo which return ^{AUT:ed}ed to its maximum snow albedo value at the end of the melting season (0.8), which ^{AUT:is was}not the case ^{AUT:oin}in the observations. Concerning 490 simulated albedo, it ^{AUT:globally mostly}follow ^{AUT:s}the observations, however, ^{AUT:it is clear that}the snow age parameterisation in

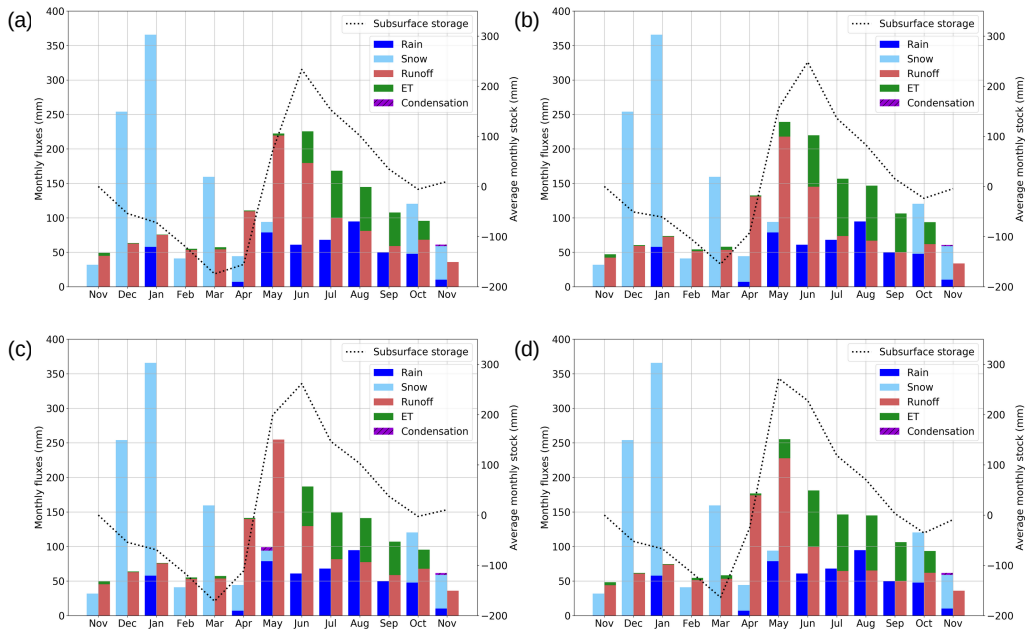


Figure 8. Same figure as 5b for (a) all distributed run (2D-AD), (b) only precipitation distributed run (2D-PD), (c) only shortwave radiation distributed run (2D-SD) and (d) only wind speed distributed run (2D-WD).

the model ^{AUT:}iswas not adequate enough to simulate the albedo where observation show ^{AUT:}s albedo decrease during melting period ^{AUT:}s.

In the 2D-AD simulation ^{AUT:}patchiness startsthe snow cover becomes discontinuous early in May and some ^{AUT:}snow-cover-pixels last up to more than one month laterpixels stay covered with snow more than one month later compared to the 1D-PM simulation (Fig. 9a). ^{AUT:}Depth variability increases during snow accumulation events and is slightly reduced during meltingSnow depth variability in the watershed, as indicated by the height of the shading in figure 9a, increases during the snow accumulation period, then diminishes during snowmelt. This effect can also be seen in the 2D-PD simulation but not in any other distributed forcing simulation (Fig. 9b). As 2D-AD and 2D-PD simulations were prescribed the same input precipitation and temperature, this means this effect (the deeper the snow, the faster the melting) ^{AUT:}iswas intrinsic to the snow scheme. ^{AUT:}AtOn the contrary, 2D-SD simulation show ^{AUT:}s a slight increase of depth variability during the melting period.

It can be observed in figure 9b that none of the individually distributed simulations ^{AUT:}haveshow longer snow cover compared to the all distributed ^{AUT:}runsimulation (Fig. 9a). It indicates that ^{AUT:}snow-variability-during-snow-accumulation-events- simulating the variability of snow deposition and transport patterns during snow accumulation was not enough to capture the actual behaviour of snow dynamics. ^{AUT:}It is the combination of ^{AUT:}bothprecipitation and shortwave radiation distributed forcing ^{AUT:}that resulted in ^{AUT:}longer snow periodsthe longer duration of the snow cover ^{AUT:}with more patchinessand the development of the typically observed patchiness at the end of the season. ^{AUT:}accountingLonger snow period resulted from the precipitation spatial variability during accumulation events and ^{AUT:}differential snow melting resulted from the shortwave radiation spatial distribution ^{AUT:}-dominance

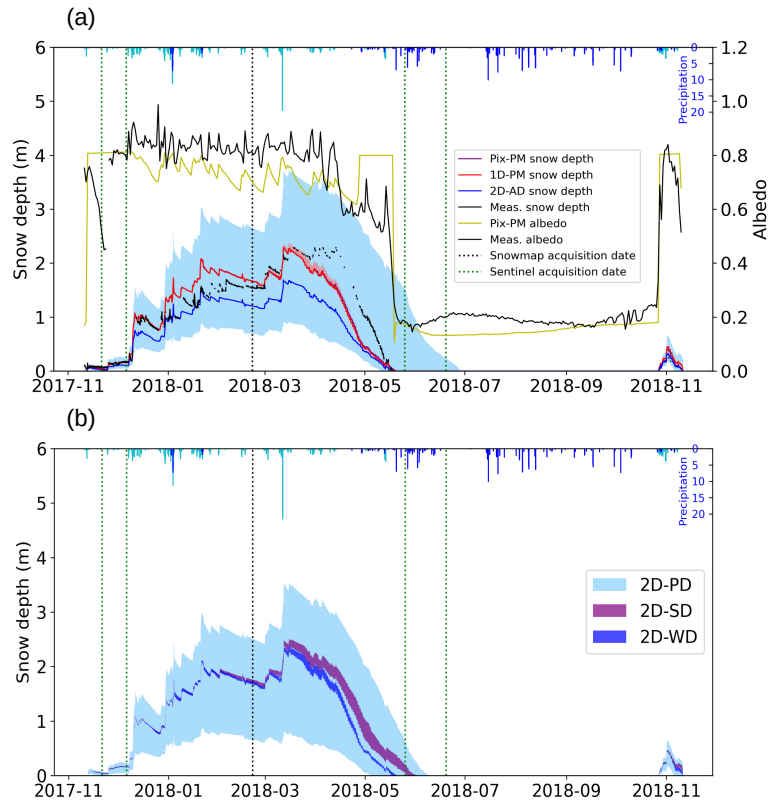


Figure 9. (a) Snow depth (left axis) for different simulations compared with observations (black line). Colour lines are the average depth over the catchment and shadings the spatial variability. Right axis: observed (black line) and 1D-PM simulated albedo (yellow line). Averaged precipitation (rain in blue and snow in cyan) are plotted at the top of the graph. (b) same as (a) but for the only precipitation (2D-PD), only shortwave radiation (2D-SD) and only wind speed (2D-WD) distributed run.

for differential snow melting. The 2D-WD simulation ^{AUT:} does not show ^{AUT:} ed ^{AUT:} much impact on the low snow depth variability which ^{AUT:} is was very similar to the 1D-PM simulation at the end of the snow ^{AUT:} accumulation period (Fig. 9b). However ^{AUT:}, along 510 spring (mid-March to end of April) it produced the same snow depth spatial variability as 2D-SD and higher snowmelt regimes (Fig. 9b and 6d). Wind speed distribution ^{AUT:} is also ^{AUT:} impacting result in snow patch ^{AUT:} iness through wind transport (accounted for in the snow distribution algorithm). In figure 9 ^{AUT:} b, the 2D-WD simulation show ^{AUT:} s ^{AUT:} a small increase in snow variability compared to 1D-PM simulation. However, the wind distribution favours more spatial dynamics when combined with other forcings.

515 Spatial distribution of snow cover during the melting period is shown on figure 10 for all simulations. ^{AUT:} For comparison and validation, we used four cloud-free 'Sentinel-2' images (Table 3). On 21st of November first snow events ^{AUT:} are were followed by a partial melting over the catchment (^{AUT:} 1st Sentinel-2 image 1st row in Fig. 10). Our 2D-AD and 2D-PD simulations ^{AUT:} are were partially good at representing this feature, but the simulated melting was overall not enough. ^{AUT:} It is interesting to see that a ^{AUT:} apart from the

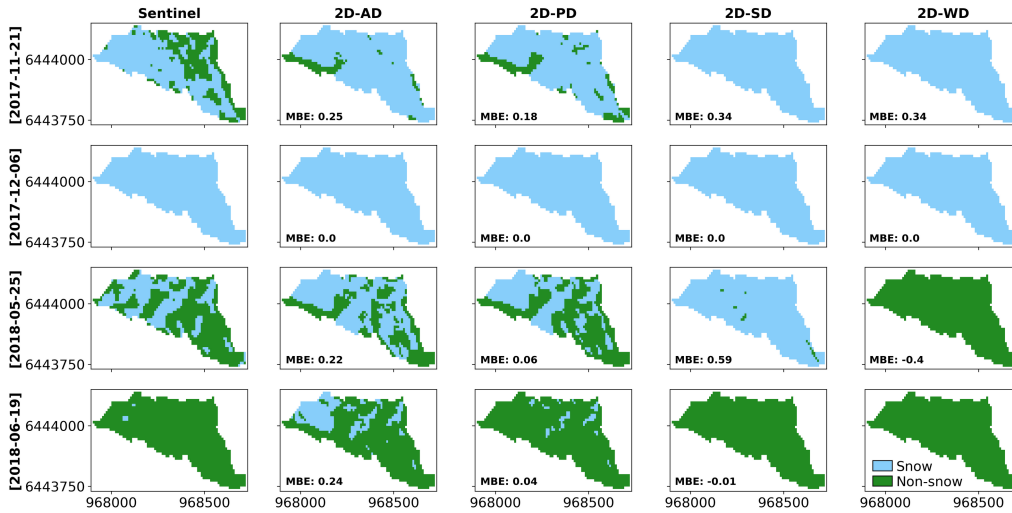


Figure 10. Snow map for different simulations compared with the Sentinel-2 images for 4 cloud free images: snow pixels (light skyblue) and non-snow pixel (green). MBE is the mean bias error between the model and Sentinel-2 image.

	Satellite platform	Date of acquisition	Resolution (m)	Cloud cover (%)	Cloud cover over catchment (%)
1	Sentinel 2B	2017-11-21	10	1.2	None
2	Sentinel 2A	2017-12-06	10	3.3	None
3	Sentinel 2A	2018-05-25	10	12.8	None
4	Sentinel 2B	2018-06-19	10	2.1	None

Table 3. Images characteristics from ESA’s Sentinel-2 mission.

upper part of the catchment where snow distribution ^{AUT:}iswas not well controlled, the ^{AUT:}first pixels that get out of snow belongs early
520 snowmelt is located to the eastern edge of the catchment, a central area aligned with the river left bank and the outlet area.
The 2D-AD simulation has ^{AUT:}lessmore snow cover than 2D-PD because of reduced incoming radiation caused by a reduced
solar angle which decrease ^{AUT:}s the melting. On 6th of December, the catchment ^{AUT:}iswas completely covered by snow for all
simulations. It has to be noted that this date corresponds to early season snow events when the 2D-AD and 2D-PD simulations
^{AUT:}arewere able to represent the snow dynamic even for very low snow depth. This means in particular that 1) our ^{AUT:}spinup
525 process has initiated well model spinup has well initialised the ground temperature profile and its distribution and 2) our distribution
algorithm ^{AUT:}iswas well adapted, especially for snow deposition. On 25th of May ^{AUT:}the catchment is partially snow covered which is
^{AUT:}specific to the advancement of melting season the snow cover has partially melted, developing kind of snow patches typical at this ad-
vanced stage of the melting season. Again 2D-PD simulation represents very well the snow pixels to non-snow pixels ratio and
the snow distribution (MBE = 0.06). One can see on both Sentinel-2 image and 2D-PD simulation some SW-NE alignment ^{AUT:};
530 slightly present on the snow distribution coefficient map (green/blue pixels on Fig. 1c), the timing of disappearance ^{AUT:}iswas

Variable	Metrics		2D-AD	2D-PD	2D-SD	2D-WD
Evapotranspiration	Slope		1.18	1.55	1.18	1.55
	R-Square		0.44	-0.36	0.44	-0.34
	RMSE		50.77	79.14	50.90	78.41
Albedo	R-Square		0.85	0.88	0.77	0.85
	RMSE		0.12	0.10	0.14	0.12
Snow cover (Sentinel-2)	MBE	21 Nov, 2017	0.25	0.18	0.34	0.34
		06 Dec, 2017	0.00	0.00	0.00	0.00
		25 May, 2018	0.22	0.06	0.59	-0.40
		19 June, 2018	0.24	0.04	-0.01	-0.01
	RMSE	21 Nov, 2017	0.63	0.65	0.58	0.58
		06 Dec, 2017	0.00	0.00	0.00	0.00
		25 May, 2018	0.74	0.75	0.78	0.63
		19 June, 2018	0.50	0.23	0.07	0.07

Table 4. Statistical metrics for observed and simulated parameters among different simulations (MBE: mean bias error, RMSE: root mean square error).

remarkably well simulated for these pixels. ^{AUT:}The 2D-AD is not as good (MBE = 0.22) because of more snow cover than the Sentinel-2 image. However, this does not mean that 2D-AD simulation is worse than 2D-PD. This will be discussed in the next section. The 2D-AD simulation has more snow cover than 2D-PD simulation and Sentinel-2 image on 25th May (MBE = 0.22). However, we showed (section 5.2.) that the 2D-AD simulation was better in simulating the snow variability and evapotranspiration compared to 2D-PD simulation.

535 The overestimation in 2D-AD simulation may come from the snow distribution scheme or the albedo scheme of CLM.

^{AUT:}Table 4 shows the performance indicators for different spatio-temporal variables in the catchment. The goodness of fit for evapotranspiration was better when we distribute shortwave radiation in the catchment. 2D-AD and 2D-SD simulations have better value of slope, R² and RMSE. Albedo simulation was more dependent on the snow stay in the catchment. Hence, the simulation where we distribute precipitation (2D-PD) showed better accountability in albedo simulation. Higher R² value for albedo in 2D-WD distribution may come from the initial accumulation of a large amount of snow. However, we have shown that snow in this simulation melts quite early compared to other simulations. Finally, precipitation distribution was more important for the spatial snow cover. However, shortwave radiation influence the late melting pattern. In the Sentinel-2 images, the higher performance of 2D-PD simulation than 2D-AD may come from the precipitation distribution itself. Looking at performance indicators together, we could see that 2D-AD was the best simulation which captured the spatial and temporal pattern of evapotranspiration and snow cover in the catchment. It means that precipitation and evapotranspiration need to be distributed together for a more accurate representation of hydrological fluxes.

540
545

6 Discussion

^{AUT:}The presented simulations disentangle the combined effects of ^{AUT:}snowprecipitation and solar radiation distributions. This makes us able to simulate ^{AUT:}a realistic patchy snow cover ^{AUT:}spatial distribution at 10 m resolution (Fig. 10) which is a commonly
550 observed phenomenon over mid-elevation mountainous catchments (Revuelto et al., 2020). ^{AUT:}The Lidar-based snow distribution map is particularly effective for its accurate prediction of distributed snow depth in mountain and forest landscapes as
recently suggested (Painter et al., 2016; Hojatimalekshah et al., 2021; Jacobs et al., 2021). ^{AUT:}We moved one step ahead in
using the Lidar map to distribute snow precipitation over the catchment in hydrological models. The all distributed simulation
(2D-AD), which encapsulate^{AUT:}s snow distribution (based on snow map) and shortwave radiation distribution ^{AUT:}(based on
555 small scale terrain)^{AUT:}based-on-slope, efficiently simulate^{AUT:}s ^{AUT:}the snow cover and evapotranspiration spatio-temporal dynam-
ics ^{AUT:}these characteristics in our test case. ^{AUT:}However, the 2D-AD simulation is not the best one in terms of spatial melting. ^{AUT:}The reduction in melt
when solar incidence is taken into account, this simulation lags the complete melt by ~20 days (Fig. 9). However, this simulation shows a ~20-day
delay in complete snowmelt due to reduced solar radiation, when the solar angle and terrain aspect are taken into account (Fig.
9). ^{AUT:}One reason could be that we might slightly overestimate snow deposition when using the snow coefficient map. Indeed,
560 the yearly spatial average amount of snow/precipitation (1442 mm) is not the same as what is measured with the gauge (1530
mm) and at the moment, we have no means to control the average value we used in this study. This leads to an uncertainty
on the cumulated snow amount that could be tuned globally with the snow coefficient map.^{AUT:}This can be seen looking at the simu-
lated snow depth at the laser scan date which clearly overestimates the laser scan observation by ~0.5 m. Another reason ^{AUT:}for might be the lack
of melting, ^{AUT:}which could come from the snow albedo calculation ^{AUT:}in ParFlow-CLM. ^{AUT:}Indeed, looking at Fig. 9, snow
565 aging reduces too much the albedo during winter months and gives an albedo too high in April when it is re-initialized to its
fresh snow value because of very small snowfall events. Those fresh snow episodes ^{AUT:}The unusual shoot-up of albedo in April lead
to a decrease in melting and subsequently higher snow depth distribution in the catchment also decreased the simulated melting in the catchment
during spring. Both of these defaults should be further corrected with an up-to-date snow scheme and a tuned snow coefficient
map for a more precise snow depth distribution.

570 ^{AUT:}Our study focuses on the impact of terrain slope and aspect on the simulated spatio-temporal dynamics of snow cover and
evapotranspiration in critical zone hydrological models, as this has become a debated issue in recent years (Rush et al., 2021;
Parsekian et al., 2021; Fan et al., 2019). ^{AUT:} However, these are not the only source of variability. Elevation based precipitation
distribution (Dahri et al., 2016; Avanzi et al., 2021; Jabot et al., 2012) ^{AUT:}and land-use based spatial evapotranspiration patterns
(Yan et al., 2018; Melton et al., 2021) ^{AUT:}have also a large impact on mountain hydrology and have been studied extensively in
575 the last few decades. In the studied catchment we considered that land use variability was not the main driver for hydrological
responses and temperature differences within the 200 m elevation gradient were partially accounted for through the laser scan
map of snow deposition. If one would like to upscale the results to larger catchments with higher land use variability and higher
elevation gradients, then temperature variability and land use variability should be accounted for together with terrain slope
and aspect.

580 ~~AUT: The results show the~~ This study shows large sensitivity of ~~AUT: E~~ evapotranspiration to incoming solar radiation corrections (decrease in regression slope from 1.55 to 1.18). In the presented results, evapotranspiration spatial average remain ~~AUT: s~~ larger than observations. The reason to overestimate ~~AUT: the~~ evapotranspiration could come from our footprint area (Oishi et al., 2008) which is not as precise as it should be. ~~AUT: However, it has been highlighted in many studies that comparing simulation of spatially heterogeneous variables with point observation is a difficult task~~ (Pradhananga and Pomeroy, 2022; Zhu et al., 2021; Iseri et al., 2021). In our case, footprint area calculation from Eddypro (Kljun et al., 2004) gave an average peak distance of ~70 m and a 90 % contribution distance of ~400 m for summer months daily hours. These distances are larger than the catchment width in the upwind direction ~~AUT: and include areas not simulated.~~ ~~AUT: Moreover, footprint area calculation is not easy on such mountainous terrain.~~ Moreover, the theoretical background of footprint calculation supposes a flat terrain with a fully developed turbulent surface layer. This is not the case in our terrain which is undulating, inducing moisture heterogeneity with some wetlands in the lowlands. For these reasons, we chose a simpler approach for ~~AUT: a~~ the first order estimation of model performance, but considering soil moisture heterogeneities ~~AUT: which consists in the presented~~ through wind direction mask (Fig. 1). ~~AUT: We hypothesize this spatial average is better than a single pixel to compare simulated evapotranspiration series with observations.~~

ParFlow-CLM is a critical zone physically based model built to ~~AUT: be very close to the~~ closely follow the physics of hydrological processes (Kuffour et al., 2020; Tran et al., 2020). This requires reliable data for forcing, ground, vegetation and hydrology to keep consistency in the model framework ~~AUT: to simulate a~~ while simulating water path with the same accuracy. We ~~AUT: then~~ chose to work ~~AUT: only~~ with local observations, from which we built distributed forcing based on the presented algorithm ~~AUT: and from which we~~ to evaluate ~~AUT: d~~ the model (Liston and Elder, 2006). The model calibration itself consisted in building the model, which means underground geometries and their associated parameters, only from observation ~~AUT: s~~ ~~AUT: are only used.~~ ~~AUT: Building a model from observation is use to enhance our ability to understand the physical processes from hydrological modeling~~ (Sidle, 2006, 2021). However, we don't have ~~AUT: spatial~~ observations for each pixel. We then built the model on assumptions ~~AUT: by supposing~~ that what we measure ~~AUT: at a place~~ is also valid for ~~AUT: similar~~ places where we do not ~~AUT: have observations~~ have measurements. Available observations then restrict ranges to tune the model once we consider embedded parameterization, which explicitly solves melting and evapotranspiration following ~~AUT: basic~~ physical laws. ~~AUT: Then~~ Finally, we forced the model with reliable observed meteorological data. From this approach, we ~~AUT: can clearly see~~ simulated the importance of snow processes and the role of incoming radiation distributions. Indeed, the model has been evaluated against the radiation budget observation (albedo), energy budget observation (latent and sensible heat fluxes), water budget terms including snow cover, the ability of the model to produce baseflow, and snowmelt timing (Table 4). Validation with Sentinel-2 images during accumulation and melting period shows that simulations ~~AUT: are very close to~~ followed the observations in terms of onset and offset of ~~AUT: snowmelt~~ snowcover. ~~AUT: Spatial distribution of snow is also reported very close to the satellite observation when slope effects are considered in precipitation and solar radiation forcing.~~

610 ~~AUT: A Last~~ The last remark about the model configuration is that the domain has a no-flow boundary condition on the sides and at the bottom of the domain ~~AUT: (Chen et al., 2022; Kollet and Maxwell, 2006).~~ ~~AUT: It restricts the option of flux leaving from the domain only through~~ ET and streamflow ~~AUT: outlet are then the only way to get the water out.~~ In other words, this means that ~~AUT: we are not simulating~~ larger scale flow paths (water that enters from the sides of the domain or that gets out through the bottom of

615 the domain) ~~AUT:are not simulated~~ ~~AUT:which is probable~~ although it may exist for high altitudinal mountainous catchments. ~~AUT:This~~ subsurface water transfer could also lead to small differences in outlet and evapotranspiration partitioning but it will not change the conclusions of this study. We started some particle tracking calculations from 3D velocity fields produced by ParFlow for our simulations. They show a very weak percolation and transfer to deep horizons. Most of the water transfers occur in the first 10 ~~AUT:mlayers.~~ ~~AUT:This subsurface water transfer could also lead to small differences in outlet and evapotranspiration partitioning but it will not change~~ ~~the conclusions of this study.~~ AUT:It further adds that the flux leaving the bottom of the domain is not so much of a concern.

~~AUT:Importance of critical zone processes in improving the understanding of hydrological cycle is strongly debated~~ (Arora et al., 2022; Wlostowski et al., 2021). ~~AUT:These processes often remain unexplored in large scale hydrological models.~~ Fan et al. (2019) ~~AUT:highlighted the inclusion of two main processes to account for in the ESMs which includes the slope/aspect effect and soil depth~~ recommended to include slope/aspect effect and soil depth in the ESMs to improve the hydrological cycle and its feedbacks on the climate. Our study contributes to this identified issue along with an algorithm to take into account surface heterogeneity. In this study, we precise how slope/aspect impact hydrological budget given spatial variability in the meteorological forcing along with surface to subsurface transfers, and how it can be successfully included in critical zone hydrological modeling. The adopted algorithm efficiently captures the surface heterogeneity in the snow cover and evapotranspiration. The same algorithm also influences the temporal distribution of snowmelt and water balance. ~~AUT:The approach of meteorological distribution and~~ cross validation from field observations and Sentinel-2 remote sensing images is also valid for subsequent years in the catch- ment. This will be presented in the companion paper to be published. This highlights the importance of slope, aspect, and curvature inclusion in hydrological studies.

7 Conclusions

Earth system models are gaining ample highlights in socio-economic impact studies. They include more and more processes, including the complete continental water cycle, but still face difficulty to parameterize small scale sub-mesh processes. These processes are crucial in mountain landscapes, both for surface hydrology and their feedback on climate. In this study, we modeled the spatial variability of the snow cover over a small mid-altitude catchment and its impact on the hydrological budget using the 3D critical-zone model ParFlow-CLM at 10 m resolution. For this purpose, we prepared distributed forcings for precipitation (that ~~AUT:include~~ mimic snow transport), incoming solar radiation (that includes differential snow melting), and wind speed to force the model. ~~AUT:We have shown that the snow lasts longer for more than a month in our modeling setup when distributing all forcings together compared to non-distributed forcing. These longer snow stays lead to an increase in streamflow, subsurface water storage, and runoff coefficients but decrease in evapotranspiration because of shorter vegetation periods. We have shown that the precipitation distribution has the largest impact on hydrological behaviour because it favours the appearance of snow patches during the melting season. Shortwave radiation distribution has a smaller effect on creating snow patches in our simulation but enhances the differential snow melting when combined with precipitation distribution. Our wind speed distributed simulation also induces melting spatial variability in the core of the melting period but reduces at the end of the melting period, as only taken into account for evapotranspiration processes. However, the wind has a major role in snow re-distribution. This is well accounted for in our precipitation distribution algorithm using a laser scan of the snow mantle during the accumulation period which registered the snow variability aligned with the prevailing wind direction.~~

Furthermore, accounting for distributed solar incidence reduces the incoming radiation in our catchment which subsequently reduces evapotranspiration. This led to higher runoff coefficients at catchment scales. In conclusion, this study shows the relative importance of small-scale processes in earth system models when run at hyper-resolution. The terrain substantially controls the hydrological behaviour over the mid-elevation alpine catchment for runoff generation, evapotranspiration, and snow dynamics, which has to be accounted for using terrain-based meteorologic forcing distribution. It will help to minimise the erratum in water resource management. The major conclusions of the study could be summarised as:

- *AUT:* Precipitation distribution (including wind redistribution) has the largest impact on driving the patchiness of the snow cover in the catchment. This leads to one month longer presence of snow in the catchment when accounting for precipitation distribution in simulations compared to simulations ignoring it.
 - *AUT:* Modulation of incoming solar radiation by the local slope in the catchment is the second most impacting topographic parametrization for melting as well as for evapotranspiration which then impact the water budget of the catchment.
 - *AUT:* Distributing wind speed according to the terrain induces some spatial variability in the simulated snowmelt at the heart of the melting period, but reduces this variability at the end of the melting period.
 - Most *AUT:* of hydrological processes are slope dependent, but it is merely taken into account in land surface and hydrological models. The study quantifies the hydrological impacts in terms of melting, streamflow, and evapotranspiration dynamic when taking into account, or not, the slope effect. Considering critical zone models applied to mountainous area, we *AUT:* believe that it is mandatory strongly recommend to consider subgrid-scale slope/aspect effects in large scale models, especially when they are used for hydrological studies. *AUT:* It will improve the spatial representation of snow processes and evapotranspiration and minimise biases in water resource management.
- AUT:* Solar radiation angle with respect to catchment slope is the second most impacting topographic parametrization for melting as well as for evapotranspiration.

Code and data availability. *AUT:* The published datasets are available at doi.org/10.18709/PERSCIDO.2022.09.DS375, which includes the ParFlow version used in the study, forcing datasets for the non-distributed and all-distributed forcing, input and TCL script to launch ParFlow. The source code for the ParFlow version used in this study is available to clone from: (<https://github.com/aniketgupta2009/treeac-alp-parflow-ver-meteo.git>).

Author contributions. A. Gupta, A. Reverdy, J-M. Cohard, designed the experiments and prepared all the necessary inputs to run the model, and A. Gupta performed the simulations. R. Maxwell and B. Hector developed the model ParFlow-CLM Model version for this study, D. Voisin processed the required meteorological data, M. Desclotres and J-P. Vandervaere provided soil and aquifer properties, C. Coulaud, L. Ligier and R. Biron manage Eddy Covariance micro-meteorological station and all field works at Lautaret Pass, J-G. Valay and D. Voisin brings the necessary support to make this study possible. A. Gupta, J-M. Cohard and D. Voisin analyzed the simulations. A. Gupta and J-M. Cohard prepared the manuscript with contributions from all co-authors.

Competing interests. The authors declare that they have no conflict of interest.

Acknowledgements. This research was conducted within the Long-Term Socio-Ecological Research (LTSER) platform Lautaret-Oisans, a site of the European Research Infrastructure eLTER. It received funding from the Lautaret Garden (Univ. Grenoble Alpes, CNRS, LAUTARET, 38000 Grenoble, France), a member of the Zone Atelier Alpes and the eLTER network and from ANR project ANR-15-IDEX-02.

References

- Aguayo, M. A., Flores, A. N., McNamara, J. P., Marshall, H.-P., and Mead, J.: Examining cross-scale influences of forcing res-
685 olutions in a hillslope-resolving, integrated hydrologic model, *Hydrology and Earth System Sciences Discussions*, pp. 1–28,
<https://doi.org/https://doi.org/10.5194/hess-2020-451>, publisher: Copernicus GmbH, 2020.
- Ajami, H., McCabe, M. F., Evans, J. P., and Stisen, S.: Assessing the impact of model spin-up on surface water-groundwater interactions
using an integrated hydrologic model, *Water Resources Research*, 50, 2636–2656, iSBN: 0043-1397 Publisher: Wiley Online Library,
2014.
- 690 Arora, B., Briggs, M. A., Zarnetske, J. P., Stegen, J., Gomez-Velez, J. D., Dwivedi, D., and Steefel, C.: Hot spots and hot moments in
the critical zone: identification of and incorporation into reactive transport models, in: *Biogeochemistry of the Critical Zone*, pp. 9–47,
Springer, 2022.
- Ashby, S. F. and Falgout, R. D.: A parallel multigrid preconditioned conjugate gradient algorithm for groundwater flow simulations, *Nuclear
science and engineering*, 124, 145–159, iSBN: 0029-5639 Publisher: Taylor & Francis, 1996.
- 695 Avanzi, F., Ercolani, G., Gabellani, S., Cremonese, E., Pogliotti, P., Filippa, G., Morra di Cella, U., Ratto, S., Stevenin, H., and Cauduro, M.:
Learning about precipitation lapse rates from snow course data improves water balance modeling, *Hydrology and Earth System Sciences*,
25, 2109–2131, iSBN: 1027-5606 Publisher: Copernicus GmbH, 2021.
- Baba, M. W., Gascoin, S., Kinnard, C., Marchane, A., and Hanich, L.: Effect of Digital Elevation Model Resolu-
tion on the Simulation of the Snow Cover Evolution in the High Atlas, *Water Resources Research*, 55, 5360–5378,
700 <https://doi.org/https://doi.org/10.1029/2018WR023789>, _eprint: <https://onlinelibrary.wiley.com/doi/pdf/10.1029/2018WR023789>, 2019.
- Bertoldi, G., Della Chiesa, S., Notarnicola, C., Pasolli, L., Niedrist, G., and Tappeiner, U.: Estimation of soil moisture patterns
in mountain grasslands by means of SAR RADARSAT2 images and hydrological modeling, *Journal of Hydrology*, 516, 245–257,
<https://doi.org/10.1016/j.jhydrol.2014.02.018>, 2014.
- Blöschl, G., Bierkens, M. F. P., Chambel, A., Cudennec, C., Destouni, G., Fiori, A., Kirchner, J. W., McDonnell, J. J., Savenije, H. H. G.,
705 Sivapalan, M., Stump, C., Toth, E., Volpi, E., Carr, G., Lupton, C., Salinas, J., Széles, B., Viglione, A., Aksoy, H., Allen, S. T., Amin,
A., Andréassian, V., Arheimer, B., Aryal, S. K., Baker, V., Bardsley, E., Barendrecht, M. H., Bartosova, A., Batelaan, O., Berghuijs,
W. R., Beven, K., Blume, T., Bogaard, T., Amorim, P. B. d., Böttcher, M. E., Boulet, G., Breinl, K., Brilly, M., Brocca, L., Buytaert,
W., Castellarin, A., Castelletti, A., Chen, X., Chen, Y., Chen, Y., Chiffard, P., Claps, P., Clark, M. P., Collins, A. L., Croke, B., Dathe,
A., David, P. C., Barros, F. P. J. d., Rooij, G. d., Baldassarre, G. D., Driscoll, J. M., Duethmann, D., Dwivedi, R., Eris, E., Farmer,
710 W. H., Feiccabrino, J., Ferguson, G., Ferrari, E., Ferraris, S., Fersch, B., Finger, D., Foglia, L., Fowler, K., Gartsman, B., Gascoin, S.,
Gaume, E., Gelfan, A., Geris, J., Gharari, S., Gleeson, T., Glendell, M., Bevacqua, A. G., González-Dugo, M. P., Grimaldi, S., Gupta,
A. B., Guse, B., Han, D., Hannah, D., Harpold, A., Haun, S., Heal, K., Helfricht, K., Herrnegger, M., Hipsey, M., Hlaváčiková, H.,
Hohmann, C., Holko, L., Hopkinson, C., Hrachowitz, M., Illangasekare, T. H., Inam, A., Innocente, C., Istanbuloglu, E., Jarihani, B.,
Kalantari, Z., Kalvans, A., Khanal, S., Khatami, S., Kiesel, J., Kirkby, M., Knoben, W., Kochanek, K., Kohnová, S., Kolechkina, A.,
715 Krause, S., Kremer, D., Kreibich, H., Kunstmann, H., Lange, H., Liberato, M. L. R., Lindquist, E., Link, T., Liu, J., Loucks, D. P., Luce,
C., Mahé, G., Makarieva, O., Malard, J., Mashtayeva, S., Maskey, S., Mas-Pla, J., Mavrova-Guirguinova, M., Mazzoleni, M., Mernild,
S., Misstear, B. D., Montanari, A., Müller-Thomy, H., Nabizadeh, A., Nardi, F., Neale, C., Nesterova, N., Nurtaev, B., Odongo, V. O.,
Panda, S., Pande, S., Pang, Z., Papacharalampous, G., Perrin, C., Pfister, L., Pimentel, R., Polo, M. J., Post, D., Sierra, C. P., Ramos,
M.-H., Renner, M., Reynolds, J. E., Ridolfi, E., Rigon, R., Riva, M., Robertson, D. E., Rosso, R., Roy, T., Sá, J. H. M., Salvadori, G.,

- 720 Sandells, M., Schaeffli, B., Schumann, A., Scolobig, A., Seibert, J., Servat, E., Shafiei, M., Sharma, A., Sidibe, M., Sidle, R. C., Skaugen, T., Smith, H., Spiessl, S. M., Stein, L., Steinsland, I., Strasser, U., Su, B., Szolgay, J., Tarboton, D., Tauro, F., Thirel, G., Tian, F., Tong, R., Tussupova, K., Tyralis, H., Uijlenhoet, R., Beek, R. v., Ent, R. J. v. d., Ploeg, M. v. d., Loon, A. F. V., Meerveld, I. v., Nooijen, R. v., Oel, P. R. v., Vidal, J.-P., Freyberg, J. v., Vorogushyn, S., Wachniew, P., Wade, A. J., Ward, P., Westerberg, I. K., White, C., Wood, E. F., Woods, R., Xu, Z., Yilmaz, K. K., and Zhang, Y.: Twenty-three unsolved problems in hydrology (UPH) – a community perspective, *Hydrological Sciences Journal*, 64, 1141–1158, <https://doi.org/10.1080/02626667.2019.1620507>, publisher: Taylor & Francis _eprint: <https://doi.org/10.1080/02626667.2019.1620507>, 2019.
- Brutsaert, W.: The surface roughness parameterization, in: *Evaporation into the Atmosphere*, pp. 113–127, Springer, 1982.
- Chen, L., Šimůnek, J., Bradford, S. A., Ajami, H., and Meles, M. B.: A computationally efficient hydrologic modeling framework to simulate surface-subsurface hydrological processes at the hillslope scale, *Journal of Hydrology*, p. 128539, iISBN: 0022-1694 Publisher: Elsevier, 2022.
- 730 Clark, M. P., Fan, Y., Lawrence, D. M., Adam, J. C., Bolster, D., Gochis, D. J., Hooper, R. P., Kumar, M., Leung, L. R., Mackay, D. S., Maxwell, R. M., Shen, C., Swenson, S. C., and Zeng, X.: Improving the representation of hydrologic processes in Earth System Models, *Water Resources Research*, 51, 5929–5956, <https://doi.org/https://doi.org/10.1002/2015WR017096>, _eprint: <https://onlinelibrary.wiley.com/doi/pdf/10.1002/2015WR017096>, 2015.
- 735 Condon, L. E. and Maxwell, R. M.: Modified priority flood and global slope enforcement algorithm for topographic processing in physically based hydrologic modeling applications, *Computers & Geosciences*, 126, 73–83, <https://doi.org/10.1016/j.cageo.2019.01.020>, 2019.
- Costa, D., Shook, K., Spence, C., Elliott, J., Baulch, H., Wilson, H., and Pomeroy, J. W.: Predicting Variable Contributing Areas, Hydrological Connectivity, and Solute Transport Pathways for a Canadian Prairie Basin, *Water Resources Research*, 56, e2020WR027984, <https://doi.org/10.1029/2020WR027984>, publisher: John Wiley & Sons, Ltd, 2020.
- 740 Dahri, Z. H., Ludwig, F., Moors, E., Ahmad, B., Khan, A., and Kabat, P.: An appraisal of precipitation distribution in the high-altitude catchments of the Indus basin, *Science of the Total Environment*, 548, 289–306, iISBN: 0048-9697 Publisher: Elsevier, 2016.
- Dai, Y., Zeng, X., Dickinson, R. E., Baker, I., Bonan, G. B., Bosilovich, M. G., Denning, A. S., Dirmeyer, P. A., Houser, P. R., Niu, G., Oleson, K. W., Schlosser, C. A., and Yang, Z.-L.: The Common Land Model, *Bulletin of the American Meteorological Society*, 84, 1013–1024, <https://doi.org/10.1175/BAMS-84-8-1013>, publisher: American Meteorological Society Section: Bulletin of the American Meteorological Society, 2003.
- 745 Dozier, J.: Spectral signature of alpine snow cover from the Landsat Thematic Mapper, *Remote sensing of environment*, 28, 9–22, iISBN: 0034-4257 Publisher: Elsevier, 1989.
- Drusch, M., Del Bello, U., Carlier, S., Colin, O., Fernandez, V., Gascon, F., Hoersch, B., Isola, C., Laberinti, P., and Martimort, P.: Sentinel-2: ESA’s optical high-resolution mission for GMES operational services, *Remote sensing of Environment*, 120, 25–36, iISBN: 0034-4257 Publisher: Elsevier, 2012.
- 750 Dunne, T.: Relation of field studies and modeling in the prediction of storm runoff, *Journal of Hydrology*, 65, 25–48, [https://doi.org/10.1016/0022-1694\(83\)90209-3](https://doi.org/10.1016/0022-1694(83)90209-3), 1983.
- Fan, Y., Clark, M., Lawrence, D. M., Swenson, S., Band, L. E., Brantley, S. L., Brooks, P. D., Dietrich, W. E., Flores, A., Grant, G., Kirchner, J. W., Mackay, D. S., McDonnell, J. J., Milly, P. C. D., Sullivan, P. L., Tague, C., Ajami, H., Chaney, N., Hartmann, A., Hazenberg, P., 755 McNamara, J., Pelletier, J., Perket, J., Rouholahnejad-Freund, E., Wagener, T., Zeng, X., Beighley, E., Buzan, J., Huang, M., Livneh, B., Mohanty, B. P., Nijssen, B., Safeeq, M., Shen, C., Verseveld, W. v., Volk, J., and Yamazaki, D.: Hillslope Hydrology in Global Change

- Research and Earth System Modeling, *Water Resources Research*, 55, 1737–1772, <https://doi.org/https://doi.org/10.1029/2018WR023903>,
_eprint: <https://onlinelibrary.wiley.com/doi/pdf/10.1029/2018WR023903>, 2019.
- 760 Fang, X. and Pomeroy, J. W.: Diagnosis of future changes in hydrology for a Canadian Rockies headwater basin, *Hydrology and Earth
System Sciences*, 24, 2731–2754, <https://doi.org/https://doi.org/10.5194/hess-24-2731-2020>, publisher: Copernicus GmbH, 2020.
- Günther, D., Marke, T., Essery, R., and Strasser, U.: Uncertainties in Snowpack Simulations—Assessing the Impact of Model Structure, Pa-
765 rameter Choice, and Forcing Data Error on Point-Scale Energy Balance Snow Model Performance, *Water Resources Research*, 55, 2779–
2800, <https://doi.org/https://doi.org/10.1029/2018WR023403>, _eprint: <https://onlinelibrary.wiley.com/doi/pdf/10.1029/2018WR023403>,
2019.
- Hellström, M., Vermeulen, A., Mirzov, O., Sabbatini, S., Vitale, D., Papale, D., Tarniewicz, J., Hazan, L., Rivier, L., and Jones, S. D.: Near
770 Real Time Data Processing In ICOS RI, in: 2nd international workshop on interoperable infrastructures for interdisciplinary big data
sciences (it4ris 16) in the context of ieee real-time system symposium (rtss), 2016.
- Hofmeister, F., Arias-Rodriguez, L. F., Premier, V., Marin, C., Notarnicola, C., Disse, M., and Chiogna, G.: Intercomparison of Sentinel-2
and modelled snow cover maps in a high-elevation Alpine catchment, *Journal of Hydrology X*, 15, 100 123, iSBN: 2589-9155 Publisher:
775 Elsevier, 2022.
- Hojatimalekshah, A., Uhlmann, Z., Glenn, N. F., Hiemstra, C. A., Tennant, C. J., Graham, J. D., Spaete, L., Gelvin, A., Marshall, H.-P., and
McNamara, J. P.: Tree canopy and snow depth relationships at fine scales with terrestrial laser scanning, *The Cryosphere*, 15, 2187–2209,
iSBN: 1994-0416 Publisher: Copernicus GmbH, 2021.
- Horton, R. E.: The Rôle of infiltration in the hydrologic cycle, *Eos, Transactions American Geophysical Union*, 14, 446–460,
775 <https://doi.org/https://doi.org/10.1029/TR014i001p00446>, _eprint: <https://onlinelibrary.wiley.com/doi/pdf/10.1029/TR014i001p00446>,
1933.
- Hurrell, J. W., Holland, M. M., Gent, P. R., Ghan, S., Kay, J. E., Kushner, P. J., Lamarque, J.-F., Large, W. G., Lawrence, D., Lindsay, K.,
Lipscomb, W. H., Long, M. C., Mahowald, N., Marsh, D. R., Neale, R. B., Rasch, P., Vavrus, S., Vertenstein, M., Bader, D., Collins,
780 W. D., Hack, J. J., Kiehl, J., and Marshall, S.: The Community Earth System Model: A Framework for Collaborative Research, *Bulletin of
the American Meteorological Society*, 94, 1339–1360, <https://doi.org/10.1175/BAMS-D-12-00121.1>, publisher: American Meteorological
Society Section: Bulletin of the American Meteorological Society, 2013.
- Iseri, Y., Diaz, A. J., Trinh, T., Kavvas, M. L., Ishida, K., Anderson, M. L., Ohara, N., and Snider, E. D.: Dynamical downscaling of global
reanalysis data for high-resolution spatial modeling of snow accumulation/melting at the central/southern Sierra Nevada watersheds,
Journal of Hydrology, 598, 126 445, iSBN: 0022-1694 Publisher: Elsevier, 2021.
- 785 Jabot, E., Zin, I., Lebel, T., Gautheron, A., and Obléd, C.: Spatial interpolation of sub-daily air temperatures for snow and hydrologic
applications in mesoscale Alpine catchments, *Hydrological processes*, 26, 2618–2630, 2012.
- Jacobs, J. M., Hunsaker, A. G., Sullivan, F. B., Palace, M., Burakowski, E. A., Herrick, C., and Cho, E.: Snow depth mapping with unpiloted
aerial system lidar observations: a case study in Durham, New Hampshire, United States, *The Cryosphere*, 15, 1485–1500, iSBN: 1994-
0416 Publisher: Copernicus GmbH, 2021.
- 790 Jefferson, J. L. and Maxwell, R. M.: Evaluation of simple to complex parameterizations of bare ground evaporation, *Jour-
nal of Advances in Modeling Earth Systems*, 7, 1075–1092, <https://doi.org/https://doi.org/10.1002/2014MS000398>, _eprint:
<https://onlinelibrary.wiley.com/doi/pdf/10.1002/2014MS000398>, 2015.
- Jones, J. E. and Woodward, C. S.: Newton–Krylov-multigrid solvers for large-scale, highly heterogeneous, variably saturated flow problems,
Advances in Water Resources, 24, 763–774, iSBN: 0309-1708 Publisher: Elsevier, 2001.

- 795 Kljun, N., Calanca, P., Rotach, M. W., and Schmid, H. P.: A simple parameterisation for flux footprint predictions, *Boundary-Layer Meteorology*, 112, 503–523, iSBN: 1573-1472 Publisher: Springer, 2004.
- Klok, E. J., Jasper, K., Roelofsma, K. P., Gurtz, J., and Badoux, A.: Distributed hydrological modelling of a heavily glaciated Alpine river basin, *Hydrological sciences journal*, 46, 553–570, iSBN: 0262-6667 Publisher: Taylor & Francis, 2001.
- Kollet, S. J. and Maxwell, R. M.: Integrated surface–groundwater flow modeling: A free-surface overland flow boundary condition in a
800 parallel groundwater flow model, *Advances in Water Resources*, 29, 945–958, <https://doi.org/10.1016/j.advwatres.2005.08.006>, 2006.
- Kollet, S. J. and Maxwell, R. M.: Capturing the influence of groundwater dynamics on land surface processes using an integrated, distributed watershed model, *Water Resources Research*, 44, <https://doi.org/https://doi.org/10.1029/2007WR006004>, _eprint: <https://onlinelibrary.wiley.com/doi/pdf/10.1029/2007WR006004>, 2008.
- Kuffour, B. N. O., Engdahl, N. B., Woodward, C. S., Condon, L. E., Kollet, S., and Maxwell, R. M.: Simulating coupled surface–subsurface
805 flows with ParFlow v3.5.0: capabilities, applications, and ongoing development of an open-source, massively parallel, integrated hydrologic model, *Geoscientific Model Development*, 13, 1373–1397, <https://doi.org/https://doi.org/10.5194/gmd-13-1373-2020>, publisher: Copernicus GmbH, 2020.
- Liston, G. E. and Elder, K.: A Meteorological Distribution System for High-Resolution Terrestrial Modeling (MicroMet), *Journal of Hydrometeorology*, 7, 217–234, <https://doi.org/10.1175/JHM486.1>, publisher: American Meteorological Society Section: Journal of Hydrometeo-
810 rology, 2006.
- Liston, G. E., Perham, C. J., Shideler, R. T., and Chevront, A. N.: Modeling snowdrift habitat for polar bear dens, *Ecological Modelling*, 320, 114–134, <https://doi.org/10.1016/j.ecolmodel.2015.09.010>, 2016.
- Loritz, R., Hrachowitz, M., Neuper, M., and Zehe, E.: The role and value of distributed precipitation data in hydrological models, *Hydrology and Earth System Sciences*, 25, 147–167, <https://doi.org/https://doi.org/10.5194/hess-25-147-2021>, publisher: Copernicus GmbH, 2021.
- 815 Marsh, C. B., Pomeroy, J. W., Spiteri, R. J., and Wheeler, H. S.: A Finite Volume Blowing Snow Model for Use With Variable Resolution Meshes, *Water Resources Research*, 56, e2019WR025 307, <https://doi.org/https://doi.org/10.1029/2019WR025307>, _eprint: <https://onlinelibrary.wiley.com/doi/pdf/10.1029/2019WR025307>, 2020.
- Maxwell, R. M.: A terrain-following grid transform and preconditioner for parallel, large-scale, integrated hydrologic modeling, *Advances in Water Resources*, 53, 109–117, iSBN: 0309-1708 Publisher: Elsevier, 2013.
- 820 Maxwell, R. M. and Miller, N. L.: Development of a coupled land surface and groundwater model, *Journal of Hydrometeorology*, 6, 233–247, iSBN: 1525-7541, 2005.
- Meerveld, H. J. T.-v., James, A. L., McDonnell, J. J., and Peters, N. E.: A reference data set of hillslope rainfall-runoff response, Panola Mountain Research Watershed, United States, *Water Resources Research*, 44, <https://doi.org/https://doi.org/10.1029/2007WR006299>, _eprint: <https://onlinelibrary.wiley.com/doi/pdf/10.1029/2007WR006299>, 2008.
- 825 Melton, F. S., Huntington, J., Grimm, R., Herring, J., Hall, M., Rollison, D., Erickson, T., Allen, R., Anderson, M., and Fisher, J. B.: Openet: Filling a critical data gap in water management for the western united states, *JAWRA Journal of the American Water Resources Association*, iSBN: 1093-474X Publisher: Wiley Online Library, 2021.
- Nijssen, B. and Lettenmaier, D. P.: A simplified approach for predicting shortwave radiation transfer through boreal forest canopies, *Journal of Geophysical Research: Atmospheres*, 104, 27 859–27 868, <https://doi.org/https://doi.org/10.1029/1999JD900377>, _eprint: <https://onlinelibrary.wiley.com/doi/pdf/10.1029/1999JD900377>, 1999.
- 830 Oishi, A. C., Oren, R., and Stoy, P. C.: Estimating components of forest evapotranspiration: a footprint approach for scaling sap flux measurements, *agricultural and forest meteorology*, 148, 1719–1732, iSBN: 0168-1923 Publisher: Elsevier, 2008.

- Oleson, K. W., Dai, Y., Bonan, G., Bosilovich, M., Dickinson, R., Dirmeyer, P., Hoffman, F., Houser, P., Levis, S., and Niu, G.-Y.: Technical description of the community land model (CLM), Tech. Note NCAR/TN-461+ STR, 2004.
- 835 Painter, T. H., Berisford, D. F., Boardman, J. W., Bormann, K. J., Deems, J. S., Gehrke, F., Hedrick, A., Joyce, M., Laidlaw, R., and Marks, D.: The Airborne Snow Observatory: Fusion of scanning lidar, imaging spectrometer, and physically-based modeling for mapping snow water equivalent and snow albedo, *Remote Sensing of Environment*, 184, 139–152, ISBN: 0034-4257 Publisher: Elsevier, 2016.
- Parsekian, A. D., Grana, D., Neves, F. d. A., Pleasants, M. S., Seyfried, M., Moravec, B. G., Chorover, J., Moraes, A. M., Smeltz, N. Y., and Westenhoff, J. H.: Hydrogeophysical comparison of hillslope critical zone architecture for different geologic substrates, *Geophysics*, 86, 840 WB29–WB49, ISBN: 0016-8033 Publisher: Society of Exploration Geophysicists, 2021.
- Pomeroy, J. W. and Li, L.: Prairie and arctic areal snow cover mass balance using a blowing snow model, *Journal of Geophysical Research: Atmospheres*, 105, 26 619–26 634, <https://doi.org/https://doi.org/10.1029/2000JD900149>, _eprint: <https://onlinelibrary.wiley.com/doi/pdf/10.1029/2000JD900149>, 2000.
- Pomeroy, J. W., Toth, B., Granger, R. J., Hedstrom, N. R., and Essery, R. L. H.: Variation in Surface Energetics during Snowmelt in a Subarctic 845 Mountain Catchment, *Journal of Hydrometeorology*, 4, 702–719, [https://doi.org/10.1175/1525-7541\(2003\)004<0702:VISED>2.0.CO;2](https://doi.org/10.1175/1525-7541(2003)004<0702:VISED>2.0.CO;2), publisher: American Meteorological Society Section: *Journal of Hydrometeorology*, 2003.
- Pomeroy, J. W., Gray, D. M., Brown, T., Hedstrom, N. R., Quinton, W. L., Granger, R. J., and Carey, S. K.: The cold regions hydrological model: a platform for basing process representation and model structure on physical evidence, *Hydrological Processes*, 21, 2650–2667, <https://doi.org/https://doi.org/10.1002/hyp.6787>, _eprint: <https://onlinelibrary.wiley.com/doi/pdf/10.1002/hyp.6787>, 2007.
- 850 Pradhananga, D. and Pomeroy, J. W.: Diagnosing changes in glacier hydrology from physical principles using a hydrological model with snow redistribution, sublimation, firnification and energy balance ablation algorithms, *Journal of Hydrology*, 608, 127 545, ISBN: 0022-1694 Publisher: Elsevier, 2022.
- Revuelto, J., Azorin-Molina, C., Alonso-González, E., Sanmiguel-Vallelado, A., Navarro-Serrano, F., Rico, I., and López-Moreno, J. I.: Meteorological and snow distribution data in the Izas Experimental Catchment (Spanish Pyrenees) from 2011 to 2017, *Earth System 855 Science Data*, 9, 993–1005, <https://doi.org/https://doi.org/10.5194/essd-9-993-2017>, publisher: Copernicus GmbH, 2017.
- Revuelto, J., Billecocq, P., Tuzet, F., Cluzet, B., Lamare, M., Larue, F., and Dumont, M.: Random forests as a tool to understand the snow depth distribution and its evolution in mountain areas, *Hydrological Processes*, 34, 5384–5401, <https://doi.org/https://doi.org/10.1002/hyp.13951>, _eprint: <https://onlinelibrary.wiley.com/doi/pdf/10.1002/hyp.13951>, 2020.
- Riggs, G., Hall, D., and Salomonson, V.: A snow index for the Landsat Thematic Mapper and Moderate Resolution Imaging Spectroradiometer, in: *Proceedings of IGARSS '94 - 1994 IEEE International Geoscience and Remote Sensing Symposium*, vol. 4, pp. 1942–1944 vol.4, 860 <https://doi.org/10.1109/IGARSS.1994.399618>, 1994.
- Rush, M., Rajaram, H., Anderson, R. S., and Anderson, S. P.: Modeling Aspect-Controlled Evolution of Ground Thermal Regimes on Montane Hillslopes, *Journal of Geophysical Research: Earth Surface*, 126, e2021JF006 126, ISBN: 2169-9003 Publisher: Wiley Online Library, 2021.
- 865 Sampaio, R. J., Rodriguez, D. A., Von Randow, C., da Silva, F. P., de Araújo, A. A. M., and Filho, O. C. R.: Sensible heat flux assessment in a complex coastal-mountain urban area in the metropolitan area of Rio de Janeiro, Brazil, *Meteorology and Atmospheric Physics*, <https://doi.org/10.1007/s00703-021-00812-2>, 2021.
- Sevruk, B. and WMO, G.: *Correction of precipitation measurements.(Proceedings)*, publisher: Zuerich (Switzerland) ETH, Geographisches Inst., 1986.

- 870 Sidle, R. C.: Field observations and process understanding in hydrology: essential components in scaling, *Hydrological Processes*, 20, 1439–1445, iSBN: 0885-6087 Publisher: John Wiley & Sons Ltd., 2006.
- Sidle, R. C.: Strategies for smarter catchment hydrology models: incorporating scaling and better process representation, *Geoscience Letters*, 8, 1–14, iSBN: 2196-4092 Publisher: Springer, 2021.
- Song, J., Miller, G. R., Cahill, A. T., Aparecido, L. M. T., and Moore, G. W.: Modeling land surface processes over a mountainous rainforest
875 in Costa Rica using CLM4.5 and CLM5, *Geoscientific Model Development*, 13, 5147–5173, <https://doi.org/https://doi.org/10.5194/gmd-13-5147-2020>, publisher: Copernicus GmbH, 2020.
- Sun, N., Wigmosta, M., Zhou, T., Lundquist, J., Dickerson-Lange, S., and Cristea, N.: Evaluating the functionality and streamflow impacts of explicitly modelling forest–snow interactions and canopy gaps in a distributed hydrologic model, *Hydrological Processes*, 32, 2128–2140, <https://doi.org/10.1002/hyp.13150>, _eprint: <https://onlinelibrary.wiley.com/doi/pdf/10.1002/hyp.13150>, 2018.
- 880 Tran, H., Zhang, J., Cohard, J.-M., Condon, L. E., and Maxwell, R. M.: Simulating Groundwater-Streamflow Connections in the Upper Colorado River Basin, *Groundwater*, 58, 392–405, <https://doi.org/https://doi.org/10.1111/gwat.13000>, _eprint: <https://onlinelibrary.wiley.com/doi/pdf/10.1111/gwat.13000>, 2020.
- van den Hurk, B., Best, M., Dirmeyer, P., Pitman, A., Polcher, J., and Santanello, J.: Acceleration of land surface model development over a decade of GLASS, *Bulletin of the American Meteorological Society*, 92, 1593–1600, iSBN: 0003-0007 Publisher: JSTOR, 2011.
- 885 Van Genuchten, M. T.: A closed-form equation for predicting the hydraulic conductivity of unsaturated soils, *Soil science society of America journal*, 44, 892–898, iSBN: 0361-5995 Publisher: Wiley Online Library, 1980.
- Vionnet, V., Brun, E., Morin, S., Boone, A., Faroux, S., Le Moigne, P., Martin, E., and Willemet, J.-M.: The detailed snowpack scheme Crocus and its implementation in SURFEX v7.2, *Geoscientific Model Development*, 5, 773–791, <https://doi.org/10.5194/gmd-5-773-2012>, 2012.
- Wlostowski, A. N., Molotch, N., Anderson, S. P., Brantley, S. L., Chorover, J., Dralle, D., Kumar, P., Li, L., Lohse, K. A., and Mallard, J. M.:
890 Signatures of hydrologic function across the critical zone observatory network, *Water Resources Research*, 57, e2019WR026 635, iSBN: 0043-1397 Publisher: Wiley Online Library, 2021.
- Yan, R., Zhang, X., Yan, S., Zhang, J., and Chen, H.: Spatial patterns of hydrological responses to land use/cover change in a catchment on the Loess Plateau, China, *Ecological Indicators*, 92, 151–160, iSBN: 1470-160X Publisher: Elsevier, 2018.
- Zhu, B., Xie, X., Lu, C., Lei, T., Wang, Y., Jia, K., and Yao, Y.: Extensive evaluation of a continental-scale high-resolution hydrological
895 model using remote sensing and ground-based observations, *Remote Sensing*, 13, 1247, iSBN: 2072-4292 Publisher: MDPI, 2021.